

Salivary gland macrophages assist tissue-resident CD8⁺ T cell immune surveillance

B. Stolp^{1,2,†}, F. Thelen^{1,†}, X. Ficht^{1,†}, L. M. Altenburger³, N. Ruef³, V. V. G. K. Inavalli^{4,5}, P. Germann^{6,7}, N. Page⁸, F. Moalli⁹, A. Raimondi⁹, K. A. Keyser¹⁰, S. M. Seyed Jafari¹¹, F. Barone¹², M. S. Dettmer¹³, D. Merkler⁸, M. Iannaccone⁹, J. Sharpe^{6,7,14}, C. Schlapbach¹¹, O. T. Fackler², U. V. Nägler^{4,5}, J. V. Stein^{3,*}

¹ Theodor Kocher Institute, University of Bern, 3012 Bern, Switzerland.

² Department for Infectious Diseases, Integrative Virology, Center for Integrative Infectious Disease Research, University Hospital Heidelberg, Im Neuenheimer Feld 344, 69120 Heidelberg, Germany.

³ Department of Oncology, Microbiology and Immunology, University of Fribourg, 1700 Fribourg, Switzerland.

⁴ University of Bordeaux, 33700 Bordeaux, France.

⁵ Interdisciplinary Institute for Neuroscience, CNRS UMR 5297, 33077 Bordeaux, France.

⁶ EMBL Barcelona, Dr. Aiguader 88, 08003 Barcelona, Spain.

⁷ Universitat Pompeu Fabra (UPF), 08002 Barcelona, Spain.

⁸ Department of Pathology and Immunology, University of Geneva, 1211 Geneva, Switzerland.

⁹ Division of Immunology, Transplantation and Infectious Diseases and Experimental Imaging Center, IRCCS San Raffaele Scientific Institute and Vita-Salute San Raffaele University, Via Olgettina 58, 20132 Milan, Italy.

¹⁰ Institute for Virology, OE5230, Hannover Medical School, Carl-Neuberg-Str. 1, 30625 Hannover, Germany.

¹¹ Department of Dermatology, Inselspital, Bern University Hospital, University of Bern, Switzerland.

¹² Institute of Inflammation and Ageing, University of Birmingham, Birmingham, United Kingdom.

¹³ Institute of Pathology, University of Bern, Switzerland.

¹⁴ Institució Catalana de Recerca i Estudis Avançats (ICREA), Pg. Lluís Companys 23, 08010 Barcelona, Spain.

[†] These authors contributed equally to this work

* To whom correspondence should be addressed

Contact: Jens V. Stein

Department of Oncology, Microbiology and Immunology

University of Fribourg

Ch. du Musée 5

CH-1700 Fribourg

email: jens.stein@unifr.ch

One sentence summary

Combined *in vitro* and *in vivo* imaging of salivary gland-resident tissue memory CD8⁺ T cells (T_{RM}) uncovers their unique migratory behavior and describes a novel accessory function of tissue macrophages to assist T_{RM} surveillance.

Abstract

Tissue macrophages and tissue resident memory CD8⁺ T cells (T_{RM}) play important roles for pathogen sensing and rapid protection of barrier tissues. To date, it is incompletely understood how these two cell types cooperate for efficient organ surveillance during homeostasis. Here, we used intravital imaging to show that T_{RM} dynamically crawled along tissue macrophages in murine submandibular salivary glands (SMG) during the memory phase following a viral infection. *Ex vivo* confined SMG T_{RM} integrated an unexpectedly wide range of migration modes: in addition to chemokine- and adhesion receptor-driven motility, SMG T_{RM} displayed a remarkable capacity of autonomous motility in the absence of chemoattractants and adhesive ligands. This unique intrinsic SMG T_{RM} motility was transmitted by friction and adaptation to microenvironmental topography through protrusion insertion into permissive gaps. Analysis of extracellular space in SMG using super-resolution shadow imaging showed discontinuous attachment of tissue macrophages to neighboring epithelial cells, offering paths of least resistance for patrolling T_{RM}. Upon tissue macrophage depletion, intraepithelial SMG T_{RM} showed decreased motility and reduced epithelial crossing events, and failed to cluster in response to local inflammatory chemokine stimuli. In sum, our data uncover a continuum of SMG T_{RM} migration modes and identify a new accessory function of tissue macrophages to facilitate T_{RM} patrolling of the complex exocrine gland architecture.

Keywords

Tissue-resident CD8⁺ T cells; non-lymphoid tissue; tissue macrophages; intravital imaging; super-resolution shadow imaging; exocrine glands; chemokines; adhesion

57 Introduction

58 Naïve CD8⁺ T cells (T_N) continuously traffic through lymphoid tissue such as peripheral lymph nodes (PLN)
 59 and spleen, where they screen antigen presenting dendritic cells (DCs) for the presence of cognate peptide-
 60 MHC (pMHC) complexes. Intravital two-photon microscopy (2PM) of peripheral lymph nodes (PLN)
 61 uncovered a high amoeboid-like T_N motility of 12-15 μm/min (1-4), facilitating their search for rare cognate
 62 pMHC-presenting DCs interspersed on a 3D stromal scaffold of fibroblastic reticular cells (FRC) (5-10).
 63 Intranodal motility is mediated by the CCR7 ligands CCL19 and CCL21 that drive F-actin polymerization at the
 64 leading edge in a Gαi-dependent manner to generate a retrograde cortical actin flow. Cortical actin flow is
 65 conveyed by the integrin LFA-1 into forward movement without generating substantial substrate adhesion
 66 (11-15).

67 During viral infections, effector CD8⁺ T cells (T_{EFF}) generated in reactive lymphoid tissue disseminate into non-
 68 lymphoid tissues (NLT) including gut, lung, genitourinary tract, and skin to eliminate infected cells. After
 69 clearance of viral antigens, part of T_{EFF} differentiate into central memory T cells (T_{CM}) and continue to patrol
 70 lymphoid organs, while others stably reside in NLT and to a minor extent in lymphoid tissue as non-
 71 recirculating, self-renewing tissue-resident memory T cells (T_{RM}). T_{RM} in gut, skin, and genitourinary tract act
 72 as “first line” sentinels that eliminate infected cells and trigger an organ-wide alert status through cytokine
 73 secretion upon pathogen re-encounter (16-21). The scanning behavior of epidermal T_{RM} has been extensively
 74 studied. These cells display characteristically elongated, dendritic shapes and move in a Gαi-dependent
 75 manner with speeds of 1-2 μm/min in proximity to the extracellular matrix (ECM)-rich basement membrane
 76 (BM) separating epidermis from dermis, i.e. in plane with the bottom keratinocyte layer (22, 23). Upon
 77 pathogen reencounter, epidermal CD8⁺ T cells follow local chemokine signals to accumulate around infected
 78 cells (24). CD8⁺ T cell accumulation is considered critical for cooperative elimination of infected stromal cells
 79 through repeated cytotoxic attacks (25). Similarly, CD8⁺ T_{RM} of the small intestine continuously patrol the
 80 absorptive epithelial layer (26).

81 T_{RM} are also present in exocrine glands of the head and neck region, including submandibular salivary glands
 82 (SMG). Salivary glands are targeted by several bacteria and viruses including human beta- and gamma-
 83 herpesviruses, which can cause disease, mostly in immunocompromised individuals (27, 28). Similar to skin

84 and gut, SMG contains epithelial tissue basally anchored onto connective tissue. However, while skin and gut
85 3D geometry is evenly layered, the SMG epithelium has an arborized structure, with acini secreting saliva
86 into intermediate and collecting ducts. The glandular epithelium is separated by a BM from the supporting
87 interstitium containing blood and lymphatic vasculature, fibroblasts and tissue macrophages (29). In tissue
88 sections, most CD8⁺ T_{RM} in SMG are localized within the abundant acini and ducts, implying a mechanism that
89 allows T_{EFF} arriving in interstitial venules to cross the BM below the epithelial compartment and develop into
90 memory T cells (30, 31). During acute inflammation of NLT, CD8⁺ T cell recruitment is driven by chemokines
91 and adhesion receptors (32). In contrast, the cellular dynamics of homeostatic T_{RM} surveillance in SMG after
92 viral infection and the involvement of tissue macrophages in this process have not been explored to date.
93 Here, we used intravital microscopy of mouse SMG in the memory phase following a systemic viral infection
94 to uncover a high baseline motility of T_{RM}, which often followed tissue macrophage topology. *Ex vivo*,
95 confinement alone in the absence of chemoattractants and adhesion receptors was sufficient to induce SMG
96 T_{RM} migration through friction- and protrusion-insertion-driven motility, which was further tuned by
97 chemokines and adhesion molecules. Using super-resolution microscopy to explore extracellular space
98 distribution in SMG, we observed discontinuous attachment of tissue macrophages to surrounding
99 epithelium, offering paths of least resistance to migrating T_{RM}. Accordingly, tissue macrophage depletion
100 resulted in a significant disruption of T_{RM} patrolling behavior. Taken together, our data uncover a new
101 accessory role for tissue macrophages to enable T_{RM} surveillance of salivary glands. Our observations suggest
102 a continuum of chemokine- and adhesion receptor-dependent and -independent migration modes and
103 topographic features facilitating this task.

104 Results

105 *Systemic viral infection leads to the establishment of T_{RM} in salivary glands*

106 We used a viral infection model for a comparative analysis of CD8⁺ T cell populations in lymphoid tissue and
 107 SMG (**Fig. 1A and Fig. S1A**). Systemic infection with lymphocytic choriomeningitis virus (LCMV)-OVA, a
 108 replication-competent, attenuated LCMV mutant expressing ovalbumin (OVA) as model antigen (33), led to
 109 transient and low viral titers in spleen on day 3 p.i. that remained below the detection limit in PLN and SMG
 110 (**Fig. S1B**). Adoptively transferred GFP⁺ OT-I CD8⁺ TCR tg T cells (which recognize the OVA₂₅₇₋₂₆₄ peptide in the
 111 context of H2-K^b) (34) underwent a prototypic expansion – contraction kinetic in spleen and PLN over the
 112 course of 30 days (**Fig. S1, C and D**). Despite the lack of detectable viral titers, OT-I T cells accumulated in
 113 SMG from day 6 p.i. onwards, with a stable population maintained until at least day 30 p.i. (**Fig. S1, C and D**).
 114 By day 30 p.i., OT-I T cells isolated from SMG but not PLN or spleen showed increased expression of CD103
 115 and CD69, while losing the KLRG-1⁺ population present on day 6 p.i. (**Fig. S1, E and F**). SMG OT-I T cells also
 116 upregulated PD-1 and CD44 surface levels (not shown), supporting the observation that most SMG CD8⁺ T
 117 cells had developed into *bona fide* T_{RM} at day 30 p.i. (35). Memory OT-I CD8⁺ T cells isolated from PLN were
 118 approximately 65% CD62L⁺ CD44^{high} T_{CM} , with the remaining population being CD62L⁻ CD44^{high} memory T cells.
 119 To take this heterogeneity into account, we refer to memory T cells isolated from PLN as T_{PLN-M} .
 120 T_{RM} establishment in SMG was also observed at ≥ 30 day after systemic VSV-OVA infection (not shown). In
 121 addition, we detected memory P14 CD8⁺ TCR tg T cells (which recognize the LCMV epitope gp₃₃₋₄₁ in the
 122 context of H2-D^b) (36) in SMG after infection with the LCMV Armstrong strain (**Fig. S2, A and B**). In sum,
 123 systemic viral infection led to the recruitment and retention of CD8⁺ T cell populations in SMG, even in the
 124 absence of detectable viral titers in this organ.

125

126 *SMG T_{RM} migration is characterized by dynamic cell shape changes*

127 We next determined the localization of T_{PLN-M} and T_{RM} in their target organs during the memory phase. Tissue
 128 sections showed that most GFP⁺ OT-I T cells in PLN and SMG were dispersed evenly in the tissue at day 30
 129 p.i. (**Fig. 1B**). In PLN, OT-I T_{PLN-M} cells localized mainly with smooth muscle actin (SMA)⁺ FRCs, whereas most
 130 OT-I T_{RM} cells in SMG were within or adjacent to EpCAM⁺ acini and ducts (**Fig. 1B**). We developed a sequential

surgery method to visualize homeostatic tissue surveillance of $T_{\text{PLN-M}}$ and T_{RM} in PLN and SMG, respectively, in the same host by 2PM (37). $T_{\text{PLN-M}}$ displayed characteristic amoeboid shapes and moved with high speeds comparable to T_{N} ($11.8 \pm 4.0 \mu\text{m}/\text{min}$, median \pm SD) (**Fig. 1, C and F to H; movie S1**). Compared to $T_{\text{PLN-M}}$, SMG T_{RM} displayed more pronounced shape changes, with several protrusions probing the microenvironment during migration, at times with thin and elongated cell bodies (**Fig. 1, D to G; movie S2**). While $T_{\text{PLN-M}}$ and T_{RM} covered large distances throughout the observation period of intravital imaging sequences (20-60 min), both populations differed in their speed and arrest coefficients, i.e. percentage of track segments with speeds $< 2.5 \mu\text{m}/\text{min}$. Thus, SMG T_{RM} were significantly slower than $T_{\text{PLN-M}}$ (**Fig. 1H**) and had higher arrest coefficients (**Fig. 1I**). Nonetheless, SMG T_{RM} retained a relatively high motility coefficient, which is a proxy of a cell's ability to scan the environment during random migration, of $> 15 \mu\text{m}^2/\text{min}$ (**Fig. 1J**). Accordingly, their median speed of $6.8 \pm 3.4 \mu\text{m}/\text{min}$ was notably higher than values reported for epidermal T_{RM} ($1-2 \mu\text{m}/\text{min}$) (22), with some cells achieving speeds of $> 12 \mu\text{m}/\text{min}$. Both $T_{\text{PLN-M}}$ and SMG T_{RM} retained a fast response to antigenic stimulation, as systemic administration of cognate peptide resulted in immediate arrest and secretion of IFN- γ (**Fig. 1, J and K; Fig. S2, C and D**).

We measured similar speeds for GFP $^{+}$ P14 T_{RM} in SMG before and after cognate peptide administration (**Fig. S2, A to D**). Furthermore, GFP $^{+}$ OT-I T cells patrolled the structurally comparable lacrimal gland (LG) in the same speed range ($7.6 \pm 4.3 \mu\text{m}/\text{min}$; median \pm SD; $n = 255$ tracks), suggesting that migration parameters of T_{RM} patrolling exocrine glands during homeostasis are independent of TCR specificity and reflect tissue properties. In sum, our data uncover a remarkably fast motility of exocrine gland-resident CD8 $^{+}$ T cells, which was characterized by dynamic shape changes.

T_{RM} migrate along tissue macrophages during SMG surveillance

To explore the microenvironmental context of exocrine gland T_{RM} migration, we used a CD11c-YFP reporter strain that labels SMG CD64 $^{+}$ F4/80 $^{+}$ tissue macrophages (29). CD11c-YFP $^{+}$ cells were also positive for the macrophage marker Iba-1, whereas some Iba-1 $^{+}$ cells were CD11c-YFP $^{\text{low/negative}}$, indicating that most but not all tissue macrophages were labeled in CD11c-YFP mice (**Fig. S3, A and B**). Confocal analysis of thick tissue sections showed that CD11c-YFP $^{+}$ tissue macrophages extended numerous protrusions from their cell bodies

throughout the SMG tissue and were located within EpCAM⁺ ducts and acini, as well as SMA⁺ perivascular structures of the interstitium (**Fig. S3C**). Most macrophage protrusions were phosphotyrosine-positive (**Fig. S3, D and E**) and enriched in F-actin (not shown), suggesting the presence of podosomes or focal adhesions at these sites.

To assess the spatial relationship between tissue macrophages and T_{RM}, we transferred GFP⁺ OT-I T cells into CD11c-YFP recipients one day prior to infection with LCMV-OVA and analyzed tissue sections by confocal microscopy in memory phase (\geq day 30 p.i.). We observed a striking spatial proximity of T_{RM} and tissue macrophages in SMG, with approximately 70% of OT-I T cells directly in contact with CD11c-YFP⁺ cells (**Fig. 2, A and B; movie S3**). The close spatial association between tissue macrophages and T_{RM} was confirmed by correlative light and electron microscopy imaging, with both cell membranes adjacent to each other (**Fig. 2C**). Electron microscopy images also highlighted the compact tissue structure of SMG, with tight junctions of acinar and ductal epithelium surrounded by a dense ECM (**Fig. 2D**).

Their spatial proximity to SMG macrophages in tissue sections raised the question whether patrolling T_{RM} migrate alongside macrophages. 2PM imaging of GFP⁺ T_{RM} in LCMV-OVA memory phase CD11c-YFP recipients indeed confirmed that T_{RM} crawled along CD11c-YFP⁺ macrophages during most of the observation period, with T_{RM} shapes often closely matching the underlying macrophage topology. This was particularly evident along thin macrophage protrusions, which T_{RM} often followed (**Fig. 2E; movie S4**). At the same time, T_{RM} protrusions occasionally detached from macrophages, apparently scanning the surrounding environment. Accordingly, we identified occasional T_{RM} track segments which were not associated with tissue macrophages. T_{RM} speeds were slightly elevated when in contact with tissue macrophages than when not (7.0 ± 5.3 versus 6.1 ± 4.8 $\mu\text{m}/\text{min}$; $p < 0.001$). Occasionally, we observed small T_{RM} clusters around tissue macrophages. Adoptively transferred CXCR3^{-/-} T_{RM} failed to accumulate at tissue macrophage clusters, suggesting the existence of local CXCL9/CXCL10 “hotspots” at these sites (**Fig. 2F**).

We examined whether the noticeable proximity between tissue macrophages and T_{RM} also occurred in other exocrine glands and species. A comparable association of T_{RM} and tissue macrophages was observed in LG after LCMV-OVA infection (**Fig. S3F**). Furthermore, CD3⁺ T cells colocalized with CD68⁺ macrophages in human parotid gland sections, both as dispersed individual cells and in clusters (**Fig. S3, G and H**). Taken together,

185 SMG T_{RM} colocalized with and moved alongside tissue macrophages during homeostatic tissue patrolling of
186 several exocrine glands.

187

188 *SMG T_{RM} motility is induced by confinement and can be tuned by external factors*

189 The close proximity of T_{RM} to tissue macrophages *in vivo* prompted us to examine the molecular factors
190 involved in this interaction. We performed quantitative PCR analysis of cytokine and chemokine expression
191 by CD11c-YFP⁺ cells sorted from SMG in steady-state, acute (day 6 p.i.) and memory phase (day 30 p.i.) of
192 LCMV-OVA infection. We observed detectable mRNA levels of the cytokines IL-1 and TNF, as well as the
193 chemokines CCL3, CCL4, CXCL2, CXCL9, CXCL10 and CXCL16 (not shown). Expression levels were similar at all
194 time points analyzed, reflecting the lack of detectable viral spread to this organ (**Fig. S1B**). Given the
195 expression of promigratory chemokines and adhesion receptors including ICAM-1 on tissue macrophages
196 (38), we examined their influence on T_{RM} migration parameters. To this end, we employed under agarose
197 assays that allow to precisely control environmental factors and provide the confinement required for T cell
198 motility (**Fig. 3A**) (15). To benchmark our system, we transferred T_N on CCL21 - and ICAM-1-coated plates as
199 surrogate lymphoid tissue microenvironment. We observed high chemokinetic T_N motility with similar speeds
200 as measured *in vivo* ($13.3 \pm 5.9 \mu\text{m}/\text{min}$) (**Fig. 3, B and C; movie S5**) (14, 15). T_{RM} showed a high motility (11.4
201 $\pm 3.0 \mu\text{m}/\text{min}$) when migrating on CXCL10 + CXCL12- and ICAM-1-coated plates, which was only slightly lower
202 than that of T_N (**Fig. 3C; movie S6**). These observations show that SMG T_{RM} respond to presence of
203 chemokines and adhesion molecules with high speeds.

204 We then examined T cell displacement on plates coated with fatty acid-free human serum albumin (HSA) and
205 thus free of chemoattractants and specific adhesion ligands. In line with previous findings (15), T_N and T_{PLN-M}
206 remained essentially immobile throughout the observation period (**Fig. 3, D to F; movies S7 and S8**). Under
207 these conditions, only 16% of T_N and 31% of T_{PLN-M} migrated faster than $3 \mu\text{m}/\text{min}$, and showed low
208 directionality (**Fig. 3, G and H**). In contrast, most SMG T_{RM} showed robust intrinsic motility on HSA-coated
209 plates despite the absence of chemoattractants and adhesion molecules (**Fig. 3, D to F; movies S7 and S8**).
210 Almost 70% of SMG T_{RM} migrated faster than $3 \mu\text{m}/\text{min}$ with high directionality, with their median speed of
211 $5.5 \mu\text{m}/\text{min}$ approaching values observed *in vivo* (**Fig. 3, G and H**). High temporal resolution imaging revealed

that migratory T_{RM} often formed several protrusions along the leading edge that appeared to probe the environment, followed by rapid displacement of the cell body along one of the protrusions (**movie S9**). Thus, unexpectedly, confinement alone was sufficient to induce spontaneous SMG T_{RM} migration, representing to the best of our knowledge the first observation of such a motility mode in resting T cells. Their speeds were increased in presence of chemokines and adhesion molecules, suggesting that external promigratory factors tune intrinsic cell motility.

Friction mediates T_{RM} migration in the absence of chemokines and ICAM-1

We set out to characterize the requirements for autonomous T_{RM} motility in under agarose assays. Reflecting the absence of chemoattractants and integrin ligands, pertussis toxin (PTx) treatment or addition of the β 1-blocking peptide RGD did not affect T_{RM} speeds in this setting (**Fig. 3I**). Although Mac-1 binds weakly to serum albumin (39), addition of anti-Mac-1 mAb did not cause a significant reduction in T_{RM} speeds (**Fig. 3I**). These observations suggested a friction-based migration mechanism (40). Friction is the resisting force when two elements slide against each other and may be composed of a number of fundamental forces. While the nature of the weak interactions between T_{RM} and migratory surface causing friction are not defined, we hypothesized that these might in part involve bivalent cations. Indeed, chelation of bivalent cations by EDTA caused a strong decrease of T_{RM} speeds under agarose (**Fig. 3I**). High temporal resolution imaging showed that despite the lack of translocation in presence of EDTA, T_{RM} continued to probe the environment via transient protrusion formation, essentially “running on the spot” (**Fig. 3, J and K, movie S10**). This behavior precipitated a loss in the motility coefficient (**Fig. 3L**). In sum, our data suggest that bivalent cation-dependent friction between T_{RM} and the confining 2D surfaces generated sufficient traction for translocation in the absence of considerable surface binding.

SMG T_{RM} insert protrusions between adjacent structures for translocation

In addition to friction-based migration, protrusion insertion has emerged in recent years as a complementary mechanism to allow cell migration without specific adhesions (40). The continuous probing of T_{RM} in presence of EDTA (**Fig. 3J**) provided an opportunity to test whether topographic features of the environment such as

narrow intercellular spaces may rescue cell motility by permitting insertion of pseudopods as mechanical “footholds” (41, 42). As a surrogate approach to re-introduce a “2.5D” environmental geometry in under agarose assays, we co-transferred a surplus of T_N together with T_{RM} and performed time-lapse imaging in the presence of EDTA and in the absence of chemoattractants and adhesion molecules (**Fig. 4A**). Remarkably, T_{RM} localized within T_N clusters frequently showed lateral displacement despite the presence of EDTA (**movies S10 and S11**). Under these conditions, T_{RM} displacement occurred through insertion of protrusions between adjacent T_N and subsequent translocation of the cell body accompanied by dynamic cell shape changes (**Fig. 4B**). T_{RM} within T_N clusters were significantly faster than isolated T_{RM} (5.8 ± 3.0 and 2.3 ± 1.7 $\mu\text{m}/\text{min}$, respectively), displayed higher directionality, and resembled in cell shape and speeds T_{RM} migrating *in vivo* (**Fig. 4C to E**). Once T_{RM} had traversed T_N clusters, they returned to their probing behavior without efficient translocation, indicating a close interdependence on physical contact and motility (**movie S10**).

We then examined whether potential residual molecular interactions between naive T cells and T_{RM} might act as drivers of migration. We therefore transferred uncoated polystyrene beads with T_{RM} in under agarose assays. These beads replaced T_N as surrogate 2.5D structures and allowed to examine protrusion insertion in the absence of potential adhesive interactions. In this setting, T_{RM} recapitulated the behavior observed within T_N clusters, showing effective cell displacement only when in contact with clusters of beads for protrusion insertion (**Fig. 4F; movie S12**). T_{RM} speeds increased to 6.4 ± 1.9 $\mu\text{m}/\text{min}$ and became more directional when in contact with beads, whereas isolated T_{RM} showed no displacement (**Fig. 4, G and H**). In this setting, we further observed that T_{RM} moved around dense bead areas, in line with a search for permissive gaps for locomotion (**movie S12**). In sum, SMG T_{RM} displayed a unique ability to migrate by adapting to topographic features of the environment through protrusion insertion and shape deformation, even in the absence of considerable friction, chemoattractants and adhesion receptors.

Residual in vivo motility of SMG T_{RM} in presence of integrin and chemokine receptor blockade

Our *in vitro* experiments raised the question to which extent external cues govern T_{RM} motility *in vivo*. We explored the molecular mechanisms underlying T_{RM} scanning of SMG, focusing on well-described canonical chemoattractant- and integrin-signaling pathways. Integrins provide traction and force transmission through

engagement of their ligands expressed by many cell types including macrophages, such as ICAM-1. SMG T_{RM} express $\alpha 1$, $\alpha 4$, αE , αL , $\beta 1$, $\beta 2$ and $\beta 7$ integrins, and low levels of αV (**Fig. S1 and 4A**). To assess their involvement in SMG T_{RM} immune surveillance, we administered a mix of integrin-blocking mAbs against the major lymphocyte integrin αL (CD11a/CD18, LFA-1), the E-cadherin ligand αE (CD103), and $\alpha 4$ (VLA-4 and $\alpha 4\beta 7$) to LCMV-OVA memory phase mice containing T_{PLN-M} and T_{RM} (**Fig. 5A**). We confirmed that mAbs were saturating surface integrins at the time point analyzed (**Fig. S4B**). We then followed OT-I T cell motility in PLN and SMG on \geq day 30 p.i., using dual surgery 2PM as described above. Integrin blockade significantly lowered T_{PLN-M} speeds from 11.7 to 8.8 $\mu m/min$ (**Fig. S4C**), similar to the decreased cell speeds of CD18-deficient T_N in lymphoid stroma (14). In contrast, T_{RM} speeds and crawling along tissue macrophages remained unaltered by this treatment (**Fig. 5, B and C; movie S13**). We did not detect Mac-1 (CD11b/CD18) expression on SMG T_{RM} by flow cytometry, and addition of anti-Mac1 mAb to the integrin blocking mix did not decrease T_{RM} speeds or guidance by tissue macrophages (not shown). Similarly, inclusion of blocking mAbs against $\alpha 1$ and αV together with αL , $\alpha 4$ and αE had no impact on T_{RM} cells speeds or association with macrophages ($6.5 \pm 2.7 \mu m/min$; $n = 68$ tracks).

Poor surface saturation of blocking anti- $\beta 1$ mAbs on OT-I T cells preempted us to assess the role of $\beta 1$ integrins for T_{RM} motility by this approach (not shown). As alternative, we directly administered the $\beta 1$ -blocking peptide RGD or the control peptide RAD through the Wharton's duct (WD) into SMG and followed its impact on T_{RM} motility parameters by 2PM. The WD channels saliva from SMG into the oral cavity and can be used to administer reagents or pathogens through retrograde duct cannulation (43). Control experiments using WD administration of OVA₂₅₇₋₂₆₄ peptide led to instantaneous arrest of T_{RM} similar to systemic injection, suggesting efficient peptide permeation of SMG by this route (not shown). While WD injection of either peptide slightly lowered T_{RM} speeds, we did not observe any impact on RGD administration on T_{RM} motility parameters as compared to control peptide (**Fig. 5D**). This reflected low $\beta 1$ integrin levels in the interface between macrophages and T_{RM} (**Fig. S4D**). Furthermore, E-cadherin levels on macrophages and T_{RM} were barely detectable in SMG tissue sections, arguing against a role for this cadherin in mediating close spatial association with tissue macrophages (**Fig. S4E**).

292 Cytokine-driven chemoattractant production plays a key role for T cell trafficking. Since the CXCR3 ligands
 293 CXCL9 and CXCL10 play a role in T_{RM} clustering in SMG (**Fig. 2F**), we co-transferred WT and CXCR3^{-/-} OT-I T
 294 cells one day prior to LCMV-OVA infection. Consistent with recent reports (44), we found that absence of
 295 CXCR3 did not impair T_{RM} formation in SMG after viral infection. Non-clustered CXCR3^{-/-} OT-I T_{RM} showed no
 296 significant differences in speeds as compared to WT T_{RM} (**Fig. 5E**), and lack of CXCR3 did not prevent T_{RM}
 297 patrolling along tissue macrophages (**Fig. 2F**).

298 To comprehensively assess a function for potential chemoattractants, we inhibited Gαi signaling by systemic
 299 PTx treatment (45) and performed 2PM analysis of OT-I T cell motility parameters on ≥ day 30 after LCMV-
 300 OVA infection. To control for inhibitor efficacy, we took advantage of the dual surgery of PLN and SMG in the
 301 same recipient. Systemic PTx administration significantly slowed T_{PLN-M} down from 11.3 μm/min in control
 302 versus 8.6 μm/min in PTx-treated recipients (**Fig. S4F**), resembling observations made with PTx-treated T_N in
 303 PLN (11, 13). Speeds were also decreased in SMG T_{RM} (from 6.6 to 5.5 μm/min) by PTx treatment (**Fig. 5F**),
 304 suggesting a role for chemoattractants in mediating high T_{RM} speeds. Nonetheless, we observed a robust
 305 residual motility and continued T_{RM} crawling along tissue macrophages in presence of PTx (**Fig. 5G, movie**
 306 **S14**). These data suggest that while Gαi-coupled receptors contribute to SMG T_{RM} motility, they are not
 307 required for T_{RM} association with tissue macrophages. Finally, since matrix metalloproteinases (MMP) play
 308 roles in cancer cell invasion, we interfered with MMP activity using the broad MMP-9, MMP-1, MMP-2, MMP-
 309 14 and MMP-7 inhibitor marimastat as described (46). Yet, MMP inhibition did not reduce T_{RM} migration
 310 compared to vehicle and rather resulted in a minor increase in speeds (not shown). Taken together, with
 311 exception of a minor effect by PTx, the *in vivo* inhibitor treatment examined here did not alter T_{RM} motility
 312 and close spatial proximity to tissue macrophages.

313 To directly assess intercellular adhesion between tissue macrophages and T_{RM} *ex vivo*, we co-incubated
 314 freshly isolated cells for 20 min and analyzed cluster formation by flow cytometry (**Fig. 5H**). As positive control
 315 for T cell association with tissue macrophages, we pre-incubated macrophages with cognate OVA₂₅₇₋₂₆₄
 316 peptide. While addition of OVA₂₅₇₋₂₆₄ to tissue macrophages induced detectable association with T_{RM}, baseline
 317 association between both populations remained low (**Fig. 5, H and I**). Finally, we performed under agarose
 318 assays in presence of tissue macrophages. On the few occasions when motile T_{RM} contacted co-plated tissue

macrophages, these contacts were mostly transient (**Fig. 5, J and K; movie S15**). Furthermore, T_{RM} did not crawl along macrophage protrusions as observed *in vivo* (**Fig. 5J**). These data suggested that T_{RM} association to macrophages occurred preferentially in the SMG microenvironment. Thus, within the technical limitations of our experimental approach, our *in vivo* and *in vitro* observations did not identify specific molecules that provide strong adhesion of SMG T_{RM} to tissue macrophages. Importantly, our data do not exclude the presence of unidentified adhesion receptors mediating T_{RM} association to tissue macrophages *in vivo*.

Discontinuous macrophage attachment within SMG

We considered that tissue microanatomy may contribute to the close spatial association between T_{RM} and tissue macrophages observed *in vivo*. Based on our observation that *ex vivo* SMG T_{RM} are able to insert protrusions into narrow spaces between adjacent structures lacking adhesion between them (**Fig. 4**), we decided to examine macrophage attachment within SMG applying the super-resolution shadow imaging microscopy (SUSHI) technique. SUSHI was originally developed to visualize the complex topology of the extracellular space (ECS) in living brain slices (47). It was used to study dynamic changes in ECS in response to a hyperosmotic challenge, which leads to cell shrinkage and ECS widening in brain tissue. Here, we adapted SUSHI imaging to acutely sliced SMG sections, which were superfused with the cell-impermeable fluorescent dye Calcein (**Fig. 6A**). Steady-state imaging revealed that the interstitium contained more ECS as compared to the tightly packed epithelium (**Fig. 6, B and C**). We reasoned that SUSHI in combination with hyperosmotic challenge could be applied to explore attachment between neighboring cells. Performing time-lapse ECS imaging, we acutely increased the osmolarity to induce cell shrinkage, which led to a strong increase of ECS in the interstitium (**movie S16**). In turn, interepithelial junctions remained relatively stable and only mildly increased their spacing under osmotic challenge, reflecting the presence of adherens and tight junctions known to link epithelial cells (**Fig. 6D**). In contrast, hyperosmolarity induced intraepithelial CD11c-YFP⁺ macrophages detachment from the adjacent epithelium (**Fig. 6, E and F**). This observation confirms previous reports that tissue macrophages do not form continuous adhesive contacts with the epithelium, unlike the extensive cell-to-cell contacts between acinar epithelial cells (48).

We then investigated the spatial arrangement of macrophage protrusions with regard to epithelial BM markers. The laminin ligand CD49f ($\alpha 6$) was prominent on the basal side of acini and to a lesser extent on ducts, which were identified by the presence of the tight junction protein ZO-1 on the luminal side. In some cases, tissue macrophages appeared to cross adjacent acini and ducts via their protrusions (**Fig. 6G**). For a detailed examination, we analyzed laminin-stained tissue sections from immunized CD11c-YFP mice. We observed in some cases macrophage protrusions penetrating between adjacent acini, or between epithelium and connective tissue, thus bridging adjacent compartments separated by BM (**Fig. 6H; movie S17**). Using correlative confocal and transmission electron microscopy, we validated that some macrophage protrusions transversed BM (**Fig. 6I**). Taken together, our data support the notion of discontinuous attachment of tissue macrophages to neighboring cells and occasional penetration of macrophage protrusions across the epithelial BM.

Depletion of tissue macrophages disrupts T_{RM} patrolling

Our observations prompted us to examine T_{RM} motility in the absence of tissue macrophages. To this end, we generated bone marrow chimera by reconstituting C57BL/6 or Ubi-GFP mice with control CD11c-YFP or CD11c-DTR bone marrow. At 6 weeks of reconstitution, we adoptively transferred GFP⁺ or DsRed⁺ OT-I T cells, followed by LCMV-OVA infection. In some experiments, we directly transferred OT-I T cells into CD11c-DTR mice and infected mice with LCMV-OVA. Both approaches allowed us to deplete CD11c⁺ macrophages by diphtheria toxin (DTx) treatment in the memory phase without affecting the unfolding of the adaptive immune response. Macrophage depletion in the memory phase had no impact on CD45⁺ and OT-I T cell numbers recovered from spleens and SMG up to one week after DTx treatment (not shown).

2PM imaging in DTx-treated mice revealed that SMG T_{RM} patrolling behavior was disrupted when macrophages were depleted (**Fig. 7A; movie S18**). T_{RM} motility was decreased, reflected by less displacement (**Fig. 7B**) and slower speeds (**Fig. 7C**). Also, we occasionally observed cells that returned and migrated back the same path within acini and ducts after macrophage depletion (**Fig. 7A**). To quantify this behavior, we developed a method to specifically retrieve U-turns from track parameters (**Fig. 7D**). This analysis confirmed that the percent of T cell tracks showing U-turns was doubled in DTx-treated CD11c-DTR SMG from 8.1 to

16.7 % of tracks (**Fig. 7E**). For comparison, PTx treatment had essentially no impact on U-turn frequency (1.15 fold increase as compared to PTx_{mut}). We observed a similar impact of macrophage depletion on T_{RM} speeds in LG (from 7.6 ± 4.3 to 5.5 ± 3.2 $\mu\text{m}/\text{min}$), with a 2.5 fold increase in U-turns (**Fig. S5**).

We next asked how impaired motility impacts organ surveillance. We generated tracks *in silico* from the data sets obtained by 2PM imaging of DTx- and control-treated SMG and assessed the average T_{RM} dwell time in a sphere of 80 μm diameter as surrogate epithelial structure (**Fig. 7D**). This analysis uncovered a nearly threefold increased sphere dwell time from 24 ± 1.8 min for control SMG to 69 ± 6.5 min (median \pm SEM) for DTx-treated CD11c-DTR SMG (**Fig. 7F**). For comparison, sphere dwell time was increased from 31 ± 1.8 min in PTx_{mut}-treated to 46 ± 2.45 min for PTx-treated SMG. Taken together, macrophage depletion disrupted motility parameters and increased the propensity of T_{RM} to make U-turns.

We investigated whether lack of macrophages may also affect T_{RM} transitions into and out of epithelium as part of the impaired motility pattern. To address this point, we developed an approach to optically separate epithelial from connective tissue. We reconstituted irradiated Ubi-GFP mice expressing GFP in all cells with CD11c-YFP bone marrow before transfer of DsRed⁺ OT-I T cells and systemic LCMV-OVA infection. We found that in these chimera, acini and ducts of surgically prepared SMG were GFP^{bright} and readily identifiable by their glandular shapes, whereas connective tissue was GFP^{low}. Using case-by-case 3D rendering of 2PM image sequences in memory phase (≥ 30 days p.i. with LCMV-OVA), we observed that DsRed⁺ T_{RM} were not restricted to individual epithelial structures but occasionally crossed between adjacent acini or between epithelial and connective tissue compartments in a bidirectional manner along macrophage protrusions (**Fig. 7G top; movie S19**). We confirmed this observation in a mouse model expressing membrane tomato and CD11c-YFP (**Fig. 7G bottom**). In total, 75% of T_{RM} transits ($n = 42$) into and out of epithelial structures occurred along macrophage protrusions (**Fig. 7H**). Given that not all tissue macrophages are YFP⁺ (**Fig. S3B**), the actual percentage of macrophage-assisted transitions may still be higher. DTx treatment of CD11c-DTR SMG reduced, but did not abolish, T_{RM} transit into or out of acini and ducts. In total, we observed 55 T_{RM} crossing events into or out of acini in CD11c-YFP versus 12 events in CD11c-DTR chimera SMG. These data corresponded to a 77% fewer crossing events per h track duration and a 71% fewer transitions per 1000 μm

track length in macrophage-depleted SMG (**Fig. 7, I and J; movie S18**). Reduced T_{RM} crossing into and out of epithelial structures was also observed when we prolonged DTx treatment for 5 days (**movie S20**).

Impaired intraorgan accumulation of SMG T_{RM} after macrophage depletion

Tissue macrophages are best characterized for their core functions of maintenance or restoration of tissue homeostasis by engulfing apoptotic cells (efferocytosis), clearing debris and initiation of repair (49-52). Accordingly, we observed massively increased numbers of infected cell foci in macrophage-depleted SMG after WD infection with murine cytomegalovirus expressing OVA and mCherry (53), as compared to SMG containing tissue macrophages (**Fig. S6, A and B**). The efferocytic function of tissue macrophages was independent of the presence of T_{RM} (**Fig. S6C**), although the latter partially suppressed viral replication as assessed by decreased mCherry intensity in viral foci (**Fig. S6D**). In support of this, we observed CD11c-YFP⁺ cells engulfing MCMV-infected cells after SMG infection (**Fig. S6, E and F**). These observations preempted the use of a viral rechallenge model to assess a function for tissue macrophages in facilitating T_{RM} patrolling. We therefore designed an alternative experiment to assess the support of SMG macrophages for T_{RM} surveillance and local cluster formation. We treated LCMV-OVA-immunized CD11c-YFP and CD11c-DTR BM chimera mice with DTx, followed one day later by local injection of the CXCR3 ligand CXCL10 into SMG (**Fig. 7K**). We also administered anti- α 4 and LFA-1 blocking mAbs that block recruitment of circulating T cells to SMG (44) but do not affect T_{RM} motility in this organ (**Fig. 5B**). At 4 h after CXCL10 administration, we isolated SMG and quantified T_{RM} enrichment in thick confocal SMG sections according to the area marked by the co-injected fluorescent marker. CXCR3^{-/-} OT-I T cells did not show accumulation in CXCL10 injection sites, supporting the specificity of chemokine-triggered clustering (49 - 63 > 500 μ m versus 60 - 68 cells/cm² cells < 500 μ m from injection site; range from two SMG each). WT OT-I T_{RM} were twofold enriched at CXCL10 injection sites, suggesting that these cells had followed a CXCL10 gradient or became retained during their surveillance path (**Fig. 7L**). In contrast, local accumulation of T_{RM} was lost when macrophages had been depleted, although T_{RM} numbers outside the site of chemokine injection remained comparable to macrophage-containing SMG (**Fig. 7L**). These data suggest a key role for SMG macrophages to assist T_{RM} patrolling within and between epithelial structures and to cluster at local inflammatory sites (**Fig. S7**).

425 Discussion

426 After clearing of pathogens, T_{RM} display a remarkable capacity to patrol heterogeneous tissues without
 427 impairing vital organ functions (16-20). Their scanning behavior evolved because T cells are MHC-restricted
 428 and hence need to physically probe membrane surfaces of immotile stromal cells. The key point of this study
 429 was to examine how these cells achieve this feat in the complex arborized epithelial structure of SMG during
 430 homeostatic immune surveillance. Our main finding is that T_{RM} mostly moved along tissue macrophages, and
 431 that depletion of macrophages impaired T_{RM} patrolling. These observations assign a new accessory role to
 432 tissue macrophages in addition to their core functions for tissue homeostasis and sentinels of infection. Our
 433 data suggest two non-exclusive options to explain macrophage guidance of T_{RM}: first, through unidentified
 434 specific adhesive interaction(s) independent of ICAM-1 and other adhesion molecules; and second, by
 435 offering paths of least resistance within the exocrine gland microenvironment for protrusion insertion by
 436 autonomously moving T cells. Our data provide evidence for the second option without discarding the first
 437 one. Reductionist *in vitro* experiments revealed that SMG T_{RM} respond to exogenous cues from
 438 chemoattractant and adhesion molecules. Remarkably, confinement alone suffices to trigger friction- and
 439 protrusion insertion-based motility without exogenous chemoattractants or adhesion molecule. We
 440 speculate that the continuum of intrinsic motility and integration of external factors permits T_{RM} to patrol
 441 these exocrine glands in homeostasis and rapidly respond to inflammatory stimuli.

442 Macrophages and T cells closely cooperate during the onset of inflammation, the effector phase and
 443 contraction through antigen presentation, cytokine secretion and effector functions such as phagocytosis.
 444 Yet, little is known whether and how these two cell types collaborate for surveillance of NLT during
 445 homeostasis. Tissue macrophages are best characterized for their core function of maintenance or
 446 restoration of tissue homeostasis by engulfing apoptotic cells, clearing debris and initiation of repair (49-52,
 447 54). A recent study has identified a role for tissue macrophages for cloaking of microlesions (55), a behavior
 448 we also observed in SMG after local laser injury (not shown). Tissue macrophages also serve as sentinels of
 449 infection, leading to cytokine secretion and leukocyte recruitment (16, 56, 57). In recent years, several non-
 450 phagocytic and non-sentinel functions were assigned to macrophages, as core functions of parenchymal
 451 parts of organs are outsourced to accessory cells. Accessory macrophage functions include blood vessel and

452 mammary duct morphogenesis, hematopoietic stem cell maintenance, pancreatic cell specification, lipid
 453 metabolism, relay of long-distance signals during zebrafish patterning and electric conduction in the heart
 454 (58, 59). Our data suggest a novel accessory function, which is to facilitate T_{RM} patrolling within and between
 455 acini and ducts of arborized secretory epithelium.

456 Our initial assumption was that specific adhesion receptors drive T cell association with tissue macrophages,
 457 while chemoattractants fuel their high baseline motility. Tissue macrophage express ICAM-1 and other
 458 adhesion molecules that can serve as ligands for T cell adhesion receptors, as well as chemoattractants (38).
 459 It was therefore startling that - against our initial expectations - we were unable to find evidence for strong
 460 adhesive contacts between salivary gland macrophages and T_{RM}. The experimental systems we have used to
 461 address this point encompass *in vivo* inhibition of adhesion receptors in combination with reductionist *in*
 462 *vitro* adhesion assays. Such assays have previously been employed to identify intercellular adhesion through
 463 specific molecular interactions, such as ICAM-1-driven binding between T cells and DCs (60). It is important
 464 to note our data do not rule out the presence of specific adhesive and/or promigratory interactions between
 465 T_{RM} and tissue macrophages *in situ*. For instance, low T_{RM} binding to tissue macrophages *in vitro* may be owing
 466 to altered gene expression patterns after macrophage isolation (61). Along the same line, we have not
 467 examined talin-deficient T cells that lack functional integrins, and poor surface mAb saturation preempted
 468 an analysis of CD44 for SMG T_{RM} motility (62). Of note, PTx treatment induced a minor but significant
 469 reduction in T_{RM} speeds *in vivo*. Yet, PTx treatment had essentially no impact on U-turn frequency and
 470 movement along tissue macrophages. In line with this, recent observations suggest that guidance and
 471 adhesion do not necessarily correlate, as T_N migrate along the FRC network even in the absence of LFA-1 and
 472 CCR7 (15). The influence of the physical properties of the microenvironment is increasingly recognized to
 473 play a central role for decision-taking by migrating leukocytes (63, 64). Yet, technical limitations in recreating
 474 the complex tissue microenvironment of exocrine glands under controlled *in vitro* conditions limit the
 475 experimental scope to address this issue in a definite manner.

476 The canonical model of leukocyte migration postulates chemoattractant-stimulated F-actin polymerization
 477 at the leading edge (4). The resulting retrograde F-actin flow in turn generates traction and cell body
 478 translocation via an integrin “clutch” that binds to adhesion receptors of the ECM or on the surface of

479 neighboring cells. Although integrin-independent migration in 3D matrices has become a widely accepted
 480 concept in cell biology based on studies with cell lines and DCs (40), several studies uncovered integrin
 481 involvement during immune surveillance of skin T cells (65, 66). Thus, it remained unclear to which extent
 482 integrin-free motility occurs in primary lymphocytes, which contain less cytoplasm and surface area as
 483 compared to DCs and cell lines. Another open question was whether memory T cells from distinct anatomical
 484 locations would employ similar or tissue-specific mechanisms of host surveillance. Work by Zaid et al. has
 485 identified a critical role of G-protein-coupled receptor signaling during scanning by epidermal T_{RM} (66). Our
 486 own observations confirm that similar to T_N and T_{PLN-M} , *ex vivo* confined epidermal T_{RM} do not migrate in the
 487 absence of integrin ligands or chemoattractants (not shown). Spontaneous motility under 2D confinement
 488 appears to constitute therefore a distinctive hallmark of SMG T_{RM} not shared by other resting T cells. Isolated
 489 T_{RM} showed high intrinsic protrusive activity *in vitro*, which may reflect high F-actin turnover and/or increased
 490 Rho-ROCK-mediated actomyosin contractility. In fact, low adhesiveness under confinement induces
 491 spontaneous amoeboid motility via cortical contractility in adherent mesenchymal cell lines (67, 68),
 492 suggesting that T_{RM} may use a similar mechanism for autonomous migration *in vitro* and *in vivo*. Yet, it
 493 remains currently unknown how this unique motility program is imprinted in SNG T_{RM} and whether it is shared
 494 by tissue-resident cells from other exocrine glands.

495 Adhesion-free motility in 2D conditions has been proposed for large, blebbing carcinoma cells, based on
 496 friction mediated by a large interface between migrating cells and substrates (69). We show that 2D
 497 confinement suffices to induce T_{RM} motility through cation-dependent friction, since these cells become
 498 unable to translocate their cell bodies in presence of EDTA. Friction is composed of multiple nanoscale forces
 499 between two interfaces. For instance, electrostatic and van der Waals forces have been implicated in cell
 500 migration and non-specific adherence to substrate (63, 70, 71). As chelation of bivalent cations reduced
 501 friction below a threshold for cell translocation in our setting, electrostatic forces are likely to be relevant. In
 502 principle, cells may compensate for a lower friction by increasing the contacting surface area (72). However,
 503 lymphocytes are likely too small to generate a sufficiently large interface under these conditions. In turn, T_{RM}
 504 regained the capability to translocate in presence of EDTA when narrow spaces are created by immotile
 505 neighboring cells or beads that lack strong adhesion to each other. This motility mode correlated with

continuous changes in cell shapes owing to the intrinsic protrusion formation capacity of T_{RM} . Thus, T_{RM} continuously formed multiple simultaneous protrusions that probed the environment, leading to their insertion into permissive gaps and subsequent cell body translocation. How T_{RM} protrusions generated tractive force for cell translocation under these conditions remains incompletely understood. One possibility is that protrusions insert into gaps of the 3D environment akin to cogs of a cogwheel and transmit the necessary force for translocation through retrograde actin flow along irregularly shaped surfaces, even in the absence of adhesion receptors. In fact, this translocation mode is reminiscent of the “squeezing and flowing” mechanism proposed for DCs (73), although SMG T_{RM} do not require a chemokine gradient for displacement. We also observed that T_{RM} avoided areas of high bead density, thus choosing the path of least resistance in this mode.

The efferocytic function of tissue macrophages conceivably requires physical contact with surrounding cells to detect and phagocytose senescent or infected cells. Since salivary gland macrophages do not form continuous tight and adherens junctions with neighboring cells (48), these cells may create a path of least resistance for patrolling T_{RM} . We speculate that the flexible anchorage of macrophage protrusions between epithelial cells may facilitate the insertion of F-actin-rich pseudopods by T_{RM} before squeezing of the nucleus as biggest organelle (40, 42, 74). T_{RM} migration along macrophages may be further assisted by unknown adhesion receptors or other molecular interactions between these cells. In any event, the non-proteolytic path finding is beneficial to preserve the integrity of the target tissue, as it does not require constant repair of newly generated discontinuities in the ECM (75). The scanning strategy adopted by T_{RM} resembles the migration pattern of T cell blasts in 3D collagen networks, where these cells routinely bypass dense collagen areas, while probing the environment for permissive gaps for cell body translocation (76). In fact, leukocytes have recently been shown to use the nucleus to identify the path of least resistance in complex 3D environments with different pore sizes (64). This migration mode preserves tissue integrity is energetically favorable by avoiding ECM degradation.

Reflecting the multiple functions of tissue macrophages, depletion studies make the interpretation of the physiological function of macrophage-assisted T_{RM} surveillance of SMG experimentally difficult to dissect. As example, when we locally infected macrophage-depleted SMG with MCMV, we observed massively increased

533 numbers of viral foci as compared to control SMG owing to a lack of efferocytosis. Our local CXCL10
534 deposition experiment in combination with impaired recruitment of circulating T cells suggests that
535 macrophages facilitate local T_{RM} accumulation at sites where inflammatory chemokines are produced. This
536 resembles observations made in skin infection models where CXCR3 promotes $CD8^+$ T cell accumulation at
537 sites of viral replication necessary for efficient elimination of infected cells (21, 77). A recent study by Förster
538 and colleagues has uncovered an unexpectedly low killing rate of cytotoxic T cells against viral-infected
539 stromal cells (78). Thus, effective stromal cell elimination requires cooperativity through repeated cytotoxic
540 attacks by multiple $CD8^+$ T cells. Conceivably, the promigratory accessory function of tissue macrophages
541 described here helps to cluster a quorum of T_{RM} for successful stromal cell killing. Furthermore, unlike the
542 monoclonal T_{RM} population created in our experimental setting, not all T_{RM} recognize the same pathogen
543 under physiological conditions. This might impose a requirement for T cells to scan local sites of pathogen
544 re-emergence and to form clusters for timely elimination of fast-replicating microbes.

545 In sum, our data assign a previously unnoticed interplay between tissue-resident innate and adaptive
546 immune cell populations. These findings further suggest a noticeable capacity of SMG T_{RM} to integrate a
547 continuum of intrinsic and external signals, friction and 3D structures for efficient motility, providing these
548 cells with maximal flexibility for NLT surveillance. We propose that such a mode of tissue patrolling is ideally
549 adapted to the arborized epithelial architecture of exocrine glands by permitting homeostatic surveillance
550 while maintaining responsiveness to local inflammatory cues.

551 **Materials and Methods**

552 *Mice*

553 OT-I TCR (34) and P14 TCR transgenic mice (36) were backcrossed to Tg(UBC-GFP)30Scha “Ubi-GFP” (79) or
 554 hCD2-dsRed (80) mice. Ubi-GFP (GFP⁺) OT-I mice backcrossed to CXCR3^{-/-} mice have been described (81).
 555 Tg(Itgax-Venus)1Mnz CD11c-YFP (82) and Tg(Itgax-DTR/EGFP)57Lan CD11c-DTR mice were used as recipients
 556 or bone marrow donors for lethally irradiated C57BL/6 or Ubi-GFP mice. C57BL/6 mice were purchased from
 557 Janvier (AD Horst). All mice were maintained at the Department of Clinical Research animal facility of the
 558 University of Bern, at the Theodor Kocher Institute and the University of Fribourg. All animal work has been
 559 approved by the Cantonal Committees for Animal Experimentation and conducted according to federal
 560 guidelines.

561

562 *T cell transfer and viral infections*

563 CD8⁺ T cells were negatively isolated from spleen, peripheral and mesenteric lymph nodes of GFP⁺ or dsRed⁺
 564 OT-I or GFP⁺ P14 mice, using the EasySep™ Mouse CD8⁺ T cell Isolation Kit (Stem Cell Technologies). CD8⁺ T
 565 cell purity was confirmed to be > 95% by flow cytometry prior to cell transfer. 10⁴ OT-I T cells were i.v.
 566 transferred into recipient mice 24 h before i.p. infection with 10⁵ pfu LCMV-OVA (33). Experimental read-
 567 outs for the acute, cleared and memory phase of viral infection were performed 6, 15 and ≥ 30 days p.i.,
 568 respectively.

569

570 *LCMV virus titer*

571 C57BL/6 mice were infected i.p. with 10⁵ pfu LCMV-OVA and sacrificed 3 or 5 days later. PLN, spleens and
 572 SMG were harvested and organs were snap frozen in liquid nitrogen. Recombinant LCMV-OVA infectivity was
 573 measured by immunofocus assay on MC57 cells as previously described ⁹⁶.

574

575 *Antibodies and reagents*

576 Alexa633-conjugated anti-PNAd MECA79, αL-integrin FD441.8 and anti-α4-integrin PS/2 mAbs were from
 577 nanotools (Freiburg, Germany). Anti-α1-integrin Ha31/8 was from BD Bioscience, anti-α4 integrin PS/2 and

578 anti- α E integrin M290 were from BioXCell, anti- α V integrin RMV-7 was from BioLegend, and anti-Mac1 mAb
 579 M1/70 was purified from hybridoma supernatant. TexasRed-Dextran 70 kDa was from Molecular Probes.
 580 Cascade Blue (MW 10 kDa) was purchased from Invitrogen. TRITC-Dextran (MW 70 kDa) and Diphtheria Toxin
 581 whereas purchased from Sigma. Pertussis toxin (PTx) and enzymatically inactive mutant PTx (PTx_{mut}) were
 582 obtained from List Biological Laboratories. Sodium Pyruvate (100 mM; #11360-039), HEPES buffer (1M;
 583 #15630-056), Minimum essential Medium Non-essential amino acids (MEM NEAA, #11140-035), L-Glutamine
 584 (200 mM; #25030-024), PenStrep (#15140-122) and RPMI-1640 (#21875-034) were purchased from Gibco
 585 and Fetal Bovine Serum (FCS, #SV30143.03) was purchased from HyClone.

586

587 *Flow cytometry analysis*

588 PLN and spleen were harvested at the indicated time points and single cell suspensions were obtained by
 589 passing organs through cell strainers (70 μ m; Bioswistec). Red blood cell lysis was performed on splenocytes
 590 in some experiments. For analysis of SMG and LG, organs were minced and treated with 2 U/ μ l collagenase
 591 II (Worthington Biochem), 2 U/ μ l bovine DNase I (Calbiochem) and - only for intracellular stainings of
 592 cytokines – 5 μ g/ml Brefeldin A (B6542, Sigma-Aldrich) in CMR (RPMI/10% FCS/1% HEPES/1% PenStrep/2
 593 mM L-Glutamine/1 mM Sodium Pyruvate) for 30 min at 37°C, passed through a 70 μ m cell strainer and
 594 washed with PBS/5 mM EDTA. We used following reagents for flow cytometry:

Antibody	clone	company	Order number
anti-CD3-APC	145-2C11	Biolegend	100312
anti-CD8a-PE	53-6.7	BD Biosciences	553033
anti-CD8a-PerCP	53-6.7	Biolegend	100732
anti-CD8a-APC/Fire750	53-6.7	Biolegend	100766
anti-CD11a-PE	M17/4	Biolegend	101107
anti-CD11b-PE	M1/70	BD Biosciences	553311
anti-CD11c-APC	HL3	BD Biosciences	550261
anti-CD18-PE	M18/2	Biolegend	101407

anti-CD29-PE	HMβ1-1	Biolegend	102207
anti-CD44-PE	IM7	BD Biosciences	553134
anti-CD45-PerCP	30-F11	BD Bioscience	557235
anti-CD45-BV711	30-F11	Biolegend	103147
anti-CD45.1-AF488	A20	Biolegend	110718
anti-CD45R/B220-APC	RA3-6B2	Biolegend	103212
anti-CD49a-PE	HMα1	Biolegend	142603
anti-CD49b-Biotin	DX5	Biolegend	108903
anti-CD49d-PE	PS/2	Southern Biotech	1520-09L
anti-CD51-PE	RMV-7	Biolegend	104105
anti-CD64-AF647	X54-517	BD Bioscience	558539
anti-CD69-PE	H1.2F3	Biolegend	104508
anti-CD103-APC	2E7	Biolegend	121414
anti-CD103-Biotin	M290	BD Bioscience	557493
anti-β7-integrin-Biotin	FIB504	Biolegend	321209
anti-F4/80-FITC	BM8	Biolegend	123108
anti-F4/80-APC	BM8	Biolegend	123116
anti-KLRG1-PE	2F1	BD Bioscience	561621
anti-KLRG-1-PE-Cy7	2F1	Biolegend	138415
anti-KLRG1-APC	2F1	Biolegend	138411
anti-NK1.1-APC	PK136	Biolegend	108710
anti-Siglec-F-PE	E50-2440	BD Bioscience	562068
Streptavidin-APC	-	Biolegend	405207
anti-rat IgG1 K-APC	-	Biolegend	400412
armenian hamster IgG-PE	-	Biolegend	400907

595 Single cell suspensions were stained for surface antigens on ice for 30 min with the indicated antibodies and
596 washed in FACS buffer (FB; PBS/2% FCS/1 mM EDTA) or FB with 5 µg/ml Brefeldin A for intracellular cytokine

597 stainings. All sample were washed in FB after staining, and for intracellular stainings, cells were permeabilized
 598 and fixed in Cytofix/Cytoperm (#51-2090KZ, BD Biosciences) for 20 min on ice. Fixative was removed by
 599 washing with Perm/Wash buffer (#51-2091KZ, BD Biosciences) and subsequent intracellular staining steps
 600 were performed in Perm/Wash buffer. Cells were washed again prior to acquisition and at least 10^5 cells in
 601 the lymphocyte FSC/SSC gate were acquired using a FACSCalibur (BD Bioscience), LSR II (BD Bioscience), LSR
 602 II SORP Upgrade (BD Bioscience) or Attune NxT Flow cytometer (ThermoFisher). Total cell counts were
 603 obtained by measuring single cell suspensions in PKH26 reference microbeads (Sigma) for 1 min at high
 604 speed. Gating for CD103⁺ and KLRG1⁺ was set according to isotype controls. For CD69 staining, positive and
 605 negative gates were set according to distinguishable populations and FMO was subtracted from the final %
 606 of CD69⁺ cells as background.

607

608 *Immunofluorescence*

609 Mice were anesthetized with i.p. injection of ketamine and xylazine and perfused with ice-cold 1% PFA.
 610 Organs were harvested and fixed overnight in 2% PFA prior to embedding in TissueTek O.C.T. compound
 611 (Sakura) for cryostat sectioning or 5% low-melting-point agarose (Sigma) for vibratome (Microslicer™ DTK-
 612 1000) sectioning. 6 µm-thick frozen cryostat sections were permeabilized, blocked and stained with 0.05%
 613 Triton-X 100 in 5% skimmed milk or 0.05% Tween 20 and 3% BSA for 1h, washed 3 times with PBS/1%
 614 BSA/0.05% Tween (TBPBS) and stained with goat-anti-Iba1 1/200 (ab5076, Abcam) and anti-phosphotyrosine
 615 (pTyr) (ab179530, Abcam) for 2 h at RT prior to mounting with Fluoromount-G (Electron Microscopy
 616 Sciences).

617 For vibratome sections, 100 µm-thick section were collected in a 48-well plate and blocked with TBPBS for 2
 618 h, then blocked with F_c-block o.n. at 4°C (hybridoma supernatant; 2.4 mg/ml diluted 1/800 in TBPBS). After
 619 washing once with TBPBS for 1 h, sections were stained in TBPBS for 2-3 days at 4°C (in 100 µl, 3 sections per
 620 well) with Alexa647-conjugated anti-EpCAM (1/160 dilution; clone G8.8, 118212, Biolegend), eFluor660-
 621 conjugated anti-E-cadherin (1/200 dilution; clone DECMA-1, 50-3249-1633, eBioscience), polyclonal rabbit
 622 anti-Laminin (1/1000 dilution; Z0097, Dako) or Cy3-conjugated anti-α-smooth muscle cell actin (clone 1A4,
 623 C6198, Sigma). Sections were washed 3 times for 1 h with TBPBS and incubated with secondary Cy3-

conjugated anti-rabbit Ig (1/400 in TBPBS; 111-165-144, Jackson Immune Research), then washed 3 times 1 h with TBPBS and one time with PBS. Images were acquired with a Zeiss LSM510 or Leica SP5 confocal microscope and processed using Adobe Photoshop CS6 and Imaris 8.4.1. We used Imaris software for surface rendering and channel masking function to separate fluorophores with close emission spectra (i.e. GFP and YFP).

2PM image acquisition and analysis

2PM intravital imaging of the popliteal lymph node was performed as described (83). In brief, mice were anesthetized with ketamine/xylazine/acepromazine. The right popliteal lymph node was surgically exposed. Prior to recording, Alexa 633-conjugated MECA-79 (10 µg/mouse) was injected i.v. to label HEV. 2PM was performed with an Olympus BX50WI microscope equipped with a 20X Olympus (NA 0.95) or 25X Nikon (NA 1.0) objective and a TrimScope 2PM system controlled by ImSpector software (LaVisionBiotec). Some of the image series were acquired using an automated system for real-time correction of tissue drift (84). For 2-photon excitation, a Ti:sapphire laser (Mai Tai HP) was tuned to 780 or 840 nm. For 4-dimensional analysis of cell migration, 11 to 20 x-y sections with z-spacing of 2-4 µm (22-64 µm depth) were acquired every 20 s for 20-60 min; the field of view was 150-350 x 150-350 µm. Emitted light and second harmonic signals were detected through 447/55-nm, 525/50-nm, 593/40-nm and 655/40-nm bandpass filters with non-descanned detectors in case of C57BL/6 recipient mice. For CD11c-YFP⁺ recipient mice or bone marrow chimera, we used 447/55-nm, 513/20-nm, 543/30-nm and 624/30-nm bandpass filters.

For imaging of the SMG, neck and thorax of the mouse were shaved, and residual hair removed with hair removal cream (Veet). Subsequently, the animal was fixed on its back onto a custom-built SMG imaging stage and stereotactic holders were attached to the head for stabilization. A 10 x 5 mm piece of skin on the right side of the neck was excised to expose the right SMG lobe, which was micro-surgically loosened from surrounding tissue. The right SMG lobe was flipped to the right and gently immobilized in between 2 cover glasses to minimize motion artifacts from heartbeat and breathing. During the whole operation and imaging procedure tissue was kept moist. During imaging, the temperature at the SMG was monitored and kept at 37°C by a heating ring. In most experiments, mice were operated twice (for PLN and SMG) in alternating

651 order to directly compare behavior of cells in different organs of the same recipient. Prior to imaging, blood
652 vessels were labeled by i.v. injection of 400 – 600 μ g of 10 kDa Cascade-blue dextran or 70 kDa TexasRed
653 Dextran. Surgical exposure of the LG was essentially performed as for the SMG, with the mouse fixed on its
654 left flank onto the custom-built SMG imaging stage and a 10 x 5 mm piece of skin excised between the right
655 ear and eye of the mouse.

656 Sequences of image stacks were transformed into volume-rendered four-dimensional videos with Volocity
657 6.0 or Imaris 6.00-9.00 (Bitplane), which was also used for semi-automated tracking of cell motility in three
658 dimensions. Drift in image sequences was corrected using a MATLAB script recognizing 3D movement in a
659 reference channel or by using the correct drift function of Imaris. Since our filter set up does not allow
660 complete separation of GFP and YFP signals, we performed spectral unmixing of GFP and YFP using the Image
661 J plugin “Spectral_Unmixing” from Joachim Walter. Cellular motility parameters were calculated from x, y,
662 and z coordinates of cell centroids using Volocity, Imaris and MATLAB protocols. The motility coefficient, a
663 measure of the ability of a cell to move away from its starting position, was calculated from the gradient of
664 a graph of mean displacement against the square root of time. We defined U-turns as the steepest turn over
665 five steps of a track, if it is over more than 166 degrees and has a skew line distance between the first and
666 last step smaller than one mean step of the respective track (**Fig. 7D**) to exclude continuous turns. The given
667 binomial proportion 95% confidence intervals are Wilson Score intervals. We generated 100 synthetic tracks
668 of 12 h duration for each condition using a sampling strategy, which was designed to preserve the correlation
669 between velocity and turning angle and the autocorrelation of velocity and turning angle (10). We then took
670 the first timestep further than 40 μ m away from the origin of each track as simulated dwelling time in an
671 acinus of 80 μ m diameter. These analyses were performed using scientific computing packages for Python.
672 For the image series depicted in the Figures, raw 2PM data was filtered with a fine median filter (3x3x1), and
673 brightness and contrast were adjusted. Shape factors were determined by rendering and tracking cells in
674 Imaris, and manually excluding all cells that did not move along a horizontal axis. The signal from the filter
675 cells was projected into a single z-slice and the shape-factor of the 2D image calculated with Volocity.

676

677 *In vivo inhibitor treatment*

678 Gai signaling by chemokines was blocked as described previously (45). Briefly, mice were treated with 3 µg
 679 PTx or PTx_{mut} by i.p. injection 3 h prior to imaging. For depletion of CD11c-positive cells in CD11c-DTR mice
 680 or BM chimera, 4 ng/g Diphtheria Toxin (DTx) was i.p. injected 24 h prior to imaging. Depletion efficiency of
 681 CD11c⁺ cells was determined by flow cytometry and was above 98% in all organs analyzed. For the
 682 synchronous blocking of integrins, 100 µg each of the purified mAbs M290, FD441.8, M1/70 and PS/2 were
 683 injected i.v. 16 h prior to imaging. Surface saturation of blocking mAbs in PLN and SMG suspensions was
 684 determined at the end of the experiment by sample staining with or without the same mAb clones used for
 685 blocking, followed by a fluorescently labeled secondary mAb and flow cytometry. RGD peptide or as control
 686 GRADSP (RAD) peptide (SIGMA) was injected via Wharton's duct cannulation (approximately 600 nmol of
 687 either peptide in 30 µl per lobe in PBS), as described previously (43). For this procedure, mice were
 688 anesthetized with ketamine/xylazine and their upper incisors rested on a metal rod and the lower incisors
 689 pulled down with string, which kept the mouth open. With the aid of a stereomicroscope, we located the
 690 orifice of the Wharton's duct in the sublingual caruncle and inserted a pointed glass-capillary (Untreated
 691 Fused Silica Tubing - L × I.D. 3 m × 0.10 mm, #25715, Sigma). The glass capillary was connected to a Hamilton
 692 Micro-syringe (Hamilton) via fine bore polythene tubing (0.28 mm, #800/100/100, Smiths), which allowed
 693 the injection of small volumes. For inhibition of MMPs, Marimastat (#S7156) was obtained from Selleck
 694 and diluted in PBS/10% DMSO (0.2 mg/g) or the corresponding volume of PBS/10% DMSO was injected i.p.
 695 90 min before starting imaging (46). OVA₂₅₇₋₂₆₄ (#BAP-201) and gp₃₃₋₄₁ (#BAP-206) peptides were obtained
 696 from ECM microcollections and 200 µg/100 µl saline injected i.v. immediately prior to imaging or 6 - 12 h
 697 prior to organ harvest for FACS staining.

698

699 *Viral infection via Wharton's duct cannulation*

700 Wharton's duct cannulation was prepared as described above. Approximately 12500 pfu MCMV-
 701 OVA_{mCherry} (85) were injected into the Wharton's duct (WD) of DTx-treated CD11c-DTR or CD11c-YFP mice
 702 in memory phase of LCMV-OVA infection. Mice were euthanized 48 h post infection and SMG tissue fixed in
 703 4% PFA at 4°C for 12 h.

704

705 *Under agarose assays*

706 T_N were isolated from spleen and PLN of a naive mouse using CD8⁺ T cell isolation kit from Stemcell. SMG-
707 derived macrophages were isolated from uninfected CD11c-YFP mice and sorted for CD11c-YFP⁺ cells. T_{RM}
708 and T_{CM} were isolated from SMG and PLN respectively of > 30 d LCMV-OVA-infected C57BL/6 mice. Single
709 cells suspension of SMG and PLN were stained with APC-conjugated anti-KLRG1 mAb and sorted for GFP⁺ or
710 DsRED⁺ KLRG1⁻ T_{RM} and T_{PLN-M}, respectively. A 17-mm diameter circle was cut into the center of 60-mm dishes.
711 The hole was sealed from the bottom part of the dish using aquarium silicone (Marina) and a 24-mm glass
712 coverslip. After the silicone dried, we overlaid a 5 mm-high ring cut from a 15-ml falcon tube and sealed the
713 borders with low melting point paraffin. Coverslips were washed with PBS and coated with 3% human serum
714 albumin (HSA; A1653, Sigma) o.n. at 4°C or for 3 h at 37°C. In some experiments, coverslips were coated with
715 10 µg/ml fibronectin (11080938001, Roche315-02, PeproTech). Fresh medium was added every 2 days and
716 macrophages were cultured for 6-7 days. For naïve T cell migration, coverslips were coated with 20 µg/ml
717 Protein A (6500-10, BioVision) for 1 h at 37°C, washed 3 times with PBS and blocked with 1.5 % BSA for 2 h
718 at 37°C or o.n. at 4°C. After washing once with PBS, cover glasses were coated for 2 h at 37°C with 100 nM
719 recombinant ICAM1-F_C (796IC, R&D Systems) and washed 2 times with PBS. Five ml of 2 x HBSS and 10 ml of
720 2 x RPMI containing 1% HSA for T_{RM} and T_{CM} and 20% FBS for macrophage and naïve T cell experiments, were
721 mixed and heated in a water bath to 56°C. Golden agarose (100 mg; 50152, Lonza) was dissolved and heated
722 in 5 ml distilled water before adding to the prewarmed medium to give a 1% agarose mix. After cooling to
723 37°C, 500 µl of the agarose mix was added on top of the coverslip. In some cases, inhibitors were added (200
724 µg/ml PTx, 5 µg/ml anti-Mac1 mAb, 10 µM RGD or GRADSP, 2.5 mM EDTA, or 5 µg/ml Hoechst (H21492,
725 Invitrogen). After incubation for 30 min at 4°C, the dish was warmed up to 37°C before adding 1 ml of PBS
726 outside the ring to prevent agarose drying. We punched a sink hole (diameter approximately 2 mm) at the
727 side of the agarose. Sorted T cell populations were suspended in RPMI/0.5% HSA and in some cases treated
728 with 5 µg anti-Mac1, 10 µM RGD or GRADSP, and pelleted in an Eppendorf tube. Cells were resuspended in
729 the smallest possible achievable volume (ca. 5-10 µl) and 0.3 µl were injected in the opposite side from the
730 sink hole using a 2.5-µl Eppendorf pipette. In some experiments, polystyrene beads (Sigma-Aldrich, LB30 or
731 78462) were co-injected with the cells. From the sink hole surplus of medium was collected to confine cells

between the agarose and the glass slide. Time-lapse images were taken from the center of the dish using a Zeiss fluorescent microscope (AxioObserver, Zeiss).

Correlative Confocal and Transmission Electron Microscopy

Correlative confocal and transmission electron microscopy (TEM) was carried out as described (86). Briefly, CD11c-YFP mice were perfused with PBS and SMG were fixed *in situ* by left ventricle injection of 1.5% glutaraldehyde/2% PFA in 0.1 M sodium cacodylate buffer (pH 7.4). SMG were harvested and immersed in the same solution for 16 h. Fixed samples were cryoprotected in 30% sucrose prior to embedding in OCT and freezing. Thirty μm sections were cut with a CM1520 cryostat (Leica) and collected on Superfrost Plus slides (Thermo Fisher Scientific). Sections were processed for confocal imaging using PBS as mounting medium to prevent dehydration. After confocal image acquisition, the coverslips were gently removed and sections adherent to the slide were processed for TEM as described (86). Briefly, sections were postfixed using the ferrocyanide-reduced osmium-thiocarbohydrazide-osmium (R-OTO) procedure, *en bloc* stained in 1% uranyl acetate and dehydrated through increasing concentration of ethanol. Finally, sections were embedded by overlaying a BEEM capsule filled with Epoxy resin. The BEEM capsules containing the embedded sections were detached by immersing the slides in liquid nitrogen, leaving the section facing up on the resin block. The specimens were mounted on a Leica Ultracut UCT and 70-90 nm thick serial sections were collected on formvar-coated copper slot grids and imaged with a ZEISS Leo912AB Omega fitted with a 2k \times 2k bottom-mounted slow-scan Proscan camera controlled by the EsivisionPro 3.2 software. Using the florescent confocal and bright field images, the same areas were relocated in the electron microscope and several images were acquired through the different serial section. Acquired TEM images were then aligned and overlaid with the confocal images by means of the eC-CLEM Icy plugin (87).

Super-resolution shadow imaging (SUSHI)

After euthanizing mice with CO₂, submandibular salivary glands (SMG) were isolated from 8-11 weeks old C57BL6 or CD11c-YFP mice and submerged in ice-cold PBS. SMG were embedded in 4% low gelling agarose (Sigma), cut in 300 μm -thick transversal slices and submerged in cold complete RPMI medium containing:

10% FCS (Hyclone). Slices were left to recover at room temperature for 15-30 min before entering the imaging chamber of a custom-built 3D-STED microscopy setup (47). First, the positively labelled (YFP) macrophages were identified at a depth of 20-30 μm below the surface and imaged in STED mode (excitation 485 nm, depletion 597 nm, objective HC PL APO 63X/1.30 NA, Leica) with the following acquisition parameters: field of view: 200 μm X 200 μm ; pixel size: 48 nm X 48 nm; pixel dwell time: 30 μs , frame acquisition time: 20 min. The medium was exchanged in the chamber with the complete RPMI containing 400 μM Calcein dye, which was allowed for 20 - 30 min to disperse throughout the extracellular space of the tissue. Subsequently, we acquired a SUSHI image to identify a region of interest around the macrophages. We performed a hyperosmolar challenge by exchanging the chamber solution (300 μl) with high osmolar solution (350 mOsm/L), and acquired time lapse images to track changes in ECS topology with a 20-min interval between the image frames. All image analysis including morphological measurements were done on raw images using the "Plot Line Profile" function in ImageJ on structures of interest. Brightness and contrast were adjusted using the "Brightness and Contrast" function in ImageJ. It was applied for illustration purposes only and did not affect the quantitative analysis. No filtering or any other image processing was applied, other than inverting the look-up-tables (LUT). The YFP signal was used only to identify macrophages and was not recorded during subsequent imaging. Only unambiguously recognizable macrophages and ECS were analyzed. Image analysis was performed on SMG slices from two mice in two independent experiments.

776

777 *Confocal imaging of the p-Tyr signal and quantification*

Mice were perfused with PBS containing 4% paraformaldehyde, SMG were isolated and fixed in the same solution at 4°C for 18 h, followed by at least 5 h dehydration in 30% sucrose. Glands were embedded in OCT (Tissue-Tek) and cut at a thickness of 6 and 20 μm at the cryostat, flash dried and fixed with 4% PFA for 10 min at room temperature. Sections were permeabilized using 0.2% Triton X-100, blocked in 10% serum of the secondary antibody and 2% BSA containing PBS and stained with antibodies for 18 h at 4°C in the same solution, after being washed in PBS and mounted in Prolong Gold containing DAPI (Invitrogen, Carlsbad, CA). Fluorescence microscopy was performed using the LSM880 confocal microscopes with 40x oil (Plan-Apochromat 40x 1.3 Oil DIC M27) or 63x oil (Plan-Apochromat 63x 1.3 Oil DIC M27) objectives (Zeiss,

786 Oberkochen, Germany). All images were recorded using sequential excitation. The lack of spectral overlap
787 was confirmed using single fluorescing specimens and antibody specificity via secondary controls.
788 Macrophages were identified via iba-1 and the presence and location of p-Tyr signal was quantified in 7 fields
789 of view using Imaris software. Brightness and contrast were adjusted for each image individually. Gaussian
790 filters were applied using Imaris software.

791

792 *Chemokine-driven T_{RM} accumulation*

793 After 6 weeks of reconstitution with CD11c-YFP or CD11c-DTR BM, we transferred 10^4 GFP⁺ OT-I T cells and
794 infected the day after with 10^5 pfu LCMV-OVA. After ≥ 30 days p.i., mice were anesthetized one day after i.p.
795 injection of DTx (4 ng/g) as for 2PM imaging. To block immigration of cells from blood, we treated mice with
796 integrin blocking antibodies anti- α L (FD441.8) and anti- α 4 (PS/2) (each at 50 μ g/mouse; nanotools). SMG
797 was surgically exposed. Using thin glass capillaries as for Wharton's duct injection, we injected 2 μ l of a 1:1
798 mix of mCXCL10 (100 μ g/ml; R&D 466-CR-010) and Qdots₆₅₅ (0.16 μ M; Thermo Fisher Q2152MP), to obtain
799 a final mCXCL10 amount of 0.5 μ g per site of injection. After 4 h, we sacrificed the mice and harvest the SMG
800 for vibratome sectioning. Mosaic images were taken of 100 μ m-thick sections, and lobes with the highest
801 Qdot signal were analyzed by transforming the 3D image into extended 2D image, using the Z-projection
802 function of ImageJ. T_{RM} density in the surrounding area and injection area (defined as an octagon with 500
803 μ m diameter) was calculated using Imaris 8.4.1.

804

805 *Statistical analysis*

806 Two-tailed, unpaired Student's t-test, Mann-Whitney U-test, one-way ANOVA with Dunnett's multiple
807 comparisons test, Kruskal-Wallis test, or a Wilcoxon rang test was used to determine statistical significance
808 (Prism, GraphPad). Significance was set at $p < 0.05$.

809 **Acknowledgements**

810 We thank Dr. Marcus Thelen (IRB, Bellinzona) for support with confocal imaging. This work benefitted from
811 optical setups of the Microscopy Imaging Center of the University of Bern and of the BioImaging platform of
812 the University of Fribourg.

813

814 **Funding**

815 This work was funded by Swiss National Foundation (SNF) project grants 31003A_135649, 31003A_153457
816 and 31003A_172994 (to JVS), Leopoldina fellowship LPDS 2011-16 (to BS) and SFB1129 (to BS and OTF), and
817 the Novartis foundation fellowship 16C193 (to FT). PG and JS acknowledge support of the Spanish Ministry
818 of Economy and Competitiveness, “Centro de Excelencia Severo Ochoa 2013-2017” and support of the CERCA
819 Programme/Generalitat de Catalunya.

820

821 **Author contributions**

822 BS, FT and XF performed most experiments with support by LMA and NR. LMA and KI carried out SUSHI
823 imaging under supervision of UVN. PG carried out computational analysis under supervision of JS. AR and FM
824 performed correlative electron microscopy of SMG sections under supervision of MI. NP, KAK, FB, DM and
825 OTF provided vital material and support. SMSF, MSD and CS analyzed human SMG sections. BS, FT, XF and
826 JVS designed experiments and wrote the manuscript with input from all coauthors.

827

828 **Competing interests**

829 The authors declare no competing interests.

830 References

- 831 1. R. N. Germain, M. J. Miller, M. L. Dustin, M. C. Nussenzweig, Dynamic imaging of the immune
832 system: progress, pitfalls and promise. *Nature Publishing Group*. **6**, 497–507 (2006).
- 833 2. C. Sumen, T. R. Mempel, I. B. Mazo, U. H. von Andrian, Intravital microscopy: visualizing immunity in
834 context. *Immunity*. **21**, 315–329 (2004).
- 835 3. B. Breart, P. Bousso, Cellular orchestration of T cell priming in lymph nodes. *Current Opinion in*
836 *Immunology*. **18**, 483–490 (2006).
- 837 4. P. Friedl, B. Weigelin, Interstitial leukocyte migration and immune function. *Nat Immunol*. **9**, 960–
838 969 (2008).
- 839 5. M. Bajénoff *et al.*, Highways, byways and breadcrumbs: directing lymphocyte traffic in the lymph
840 node. *Trends in Immunology*. **28**, 346–352 (2007).
- 841 6. T. Katakai, K. Habiro, T. Kinashi, Dendritic Cells Regulate High-Speed Interstitial T Cell Migration in
842 the Lymph Node via LFA-1/ICAM-1. *J. Immunol*. **191**, 1188–1199 (2013).
- 843 7. M. Lee, J. N. Mandl, R. N. Germain, A. J. Yates, The race for the prize: T-cell trafficking strategies for
844 optimal surveillance. *Blood*. **120**, 1432–1438 (2012).
- 845 8. G. Bogle, P. R. Dunbar, Agent-based simulation of T-cell activation and proliferation within a lymph
846 node. *Immunol Cell Biol*. **88**, 172–179 (2009).
- 847 9. J. Textor *et al.*, Random Migration and Signal Integration Promote Rapid and Robust T Cell
848 Recruitment. *PLoS Comput Biol*. **10**, e1003752–16 (2014).
- 849 10. M. Ackerknecht *et al.*, Antigen Availability and DOCK2-Driven Motility Govern CD4+ T Cell
850 Interactions with Dendritic Cells In Vivo. *The Journal of Immunology*. **199**, 520–530 (2017).
- 851 11. T. Okada, J. G. Cyster, CC chemokine receptor 7 contributes to Gi-dependent T cell motility in the
852 lymph node. *J. Immunol*. **178**, 2973–2978 (2007).
- 853 12. T. Worbs, T. R. Mempel, J. Bölker, U. H. von Andrian, R. Förster, CCR7 ligands stimulate the
854 intranodal motility of T lymphocytes in vivo. *J. Exp. Med*. **204**, 489–495 (2007).
- 855 13. F. Asperti-Boursin, E. Real, G. Bismuth, A. Trautmann, E. Donnadieu, CCR7 ligands control basal T cell
856 motility within lymph node slices in a phosphoinositide 3-kinase-independent manner. *J. Exp. Med*.
857 **204**, 1167–1179 (2007).
- 858 14. E. Woolf *et al.*, Lymph node chemokines promote sustained T lymphocyte motility without triggering
859 stable integrin adhesiveness in the absence of shear forces. *Nat Immunol*. **8**, 1076–1085 (2007).
- 860 15. M. Hons *et al.*, Chemokines and integrins independently tune actin flow and substrate friction
861 during intranodal migration of T cells. *Nat Immunol*. **19**, 606–616 (2018).
- 862 16. N. Iijima, A. Iwasaki, A local macrophage chemokine network sustains protective tissue-resident
863 memory CD4 T cells. *Science*. **346**, 93–98 (2014).
- 864 17. J. M. Schenkel *et al.*, Resident memory CD8 T cells trigger protective innate and adaptive immune
865 responses. *Science*. **346**, 98–101 (2014).
- 866 18. G. Stry *et al.*, A mucosal vaccine against Chlamydia trachomatis generates two waves of protective
867 memory T cells. *Science*. **348**, aaa8205–aaa8205 (2015).

- 868 19. S. Ariotti *et al.*, Skin-resident memory CD8⁺ T cells trigger a state of tissue-wide pathogen alert.
869 *Science*. **346**, 101–105 (2014).
- 870 20. M. Kadoki *et al.*, Organism-Level Analysis of Vaccination Reveals Networks of Protection across
871 Tissues. *Cell*, 1–38 (2017).
- 872 21. S. Ariotti *et al.*, Subtle CXCR3-Dependent Chemotaxis of CTLs within Infected Tissue Allows Efficient
873 Target Localization. *The Journal of Immunology*. **195**, 5285–5295 (2015).
- 874 22. A. Zaid *et al.*, Persistence of skin-resident memory T cells within an epidermal niche. *Proc. Natl.*
875 *Acad. Sci. U.S.A.* **111**, 5307–5312 (2014).
- 876 23. S. Ariotti *et al.*, Tissue-resident memory CD8⁺ T cells continuously patrol skin epithelia to quickly
877 recognize local antigen. *Proceedings of the National Academy of Sciences*. **109**, 19739–19744 (2012).
- 878 24. J. W. Griffith, C. L. Sokol, A. D. Luster, Chemokines and Chemokine Receptors: Positioning Cells for
879 Host Defense and Immunity. *Annu Rev Immunol*. **32**, 659–702 (2014).
- 880 25. S. Halle, O. Halle, R. Förster, Mechanisms and Dynamics of T Cell-Mediated Cytotoxicity In Vivo.
881 *Trends Immunol*. **38**, 432–443 (2017).
- 882 26. D. P. Hoytema van Konijnenburg, D. Mucida, Intraepithelial lymphocytes. *Curr Biol*. **27**, R737–R739
883 (2017).
- 884 27. C. S. Miller *et al.*, High Prevalence of Multiple Human Herpesviruses in Saliva from Human
885 Immunodeficiency Virus-Infected Persons in the Era of Highly Active Antiretroviral Therapy. *Journal*
886 *of Clinical Microbiology*. **44**, 2409–2415 (2006).
- 887 28. Cannon MJ *et al.* Repeated measures study of weekly and daily cytomegalovirus shedding patterns
888 in saliva and urine of healthy cytomegalovirus-seropositive children. *BMC Infect Dis* (2014) **14**:569.
- 889 29. J. T. Thom, S. M. Walton, N. Torti, A. Oxenius, Salivary gland resident APCs are Flt3L- and CCR2-
890 independent macrophage-like cells incapable of cross-presentation. *Eur. J. Immunol*. **44**, 706–714
891 (2013).
- 892 30. J. T. Thom, T. C. Weber, S. M. Walton, N. Torti, A. Oxenius, The Salivary Gland Acts as a Sink for
893 Tissue-Resident Memory CD8⁺ T Cells, Facilitating Protection from Local Cytomegalovirus Infection.
894 *CellReports*, 1–13 (2015).
- 895 31. C. J. Smith, S. Caldeira-Dantas, H. Turula, C. M. Snyder, Murine CMV Infection Induces the
896 Continuous Production of Mucosal Resident T Cells. *CellReports*, 1–13 (2015).
- 897 32. U. H. von Andrian, C. R. Mackay, T-cell function and migration. Two sides of the same coin. *New*
898 *England Journal of Medicine*. **343**, 1020–1034 (2000).
- 899 33. S. M. Kallert *et al.*, Replicating viral vector platform exploits alarmin signals for potent CD8⁺ T
900 cell-mediated tumour immunotherapy. *Nat Commun*. **8**, 1–13 (2017).
- 901 34. K. A. Hogquist *et al.*, T cell receptor antagonist peptides induce positive selection. *Cell*. **76**, 17–27
902 (1994).
- 903 35. E. M. Steinert *et al.*, Quantifying Memory CD8⁺ T Cells Reveals Regionalization of
904 Immunosurveillance. *Cell*. **161**, 737–749 (2015).
- 905 36. D. Brändle *et al.*, T cell development and repertoire of mice expressing a single T cell receptor alpha
906 chain. *Eur J Immunol*. **25**, 2650–2655 (1995).

- 907 37. X. Ficht, F. Thelen, B. Stolp, J. V. Stein, Preparation of Murine Submandibular Salivary Gland for
908 Upright Intravital Microscopy. *J Vis Exp*, 1–8 (2018).
- 909 38. E. L. Gautier *et al.*, Gene-expression profiles and transcriptional regulatory pathways that underlie
910 the identity and diversity of mouse tissue macrophages. *Nat Immunol.* **13**, 1118–1128 (2012).
- 911 39. G. E. Davis, The Mac-1 and p150,95 beta 2 integrins bind denatured proteins to mediate leukocyte
912 cell-substrate adhesion. *Exp Cell Res.* **200**, 242–252 (1992).
- 913 40. E. K. Paluch, I. M. Aspalter, M. Sixt, Focal Adhesion–Independent Cell Migration. *Annu. Rev. Cell Dev.*
914 *Biol.* **32**, 469–490 (2016).
- 915 41. J. T. H. Mandeville, M. A. Lawson, F. R. Maxfield, Dynamic imaging of neutrophil migration in three
916 dimensions: mechanical interactions between cells and matrix. *J Leukoc Biol.* **61**, 188–200 (1997).
- 917 42. S. Nourshargh, P. L. Hordijk, M. Sixt, Breaching multiple barriers: leukocyte motility through venular
918 walls and the interstitium. *Nat Rev Mol Cell Biol.* **11**, 366–378 (2010).
- 919 43. M. Bombardieri *et al.*, Inducible Tertiary Lymphoid Structures, Autoimmunity, and Exocrine
920 Dysfunction in a Novel Model of Salivary Gland Inflammation in C57BL/6 Mice. *J. Immunol.* **189**,
921 3767–3776 (2012).
- 922 44. S. Woyciechowski, M. Hofmann, H. Pircher, α 4 β 1 integrin promotes accumulation of tissue-resident
923 memory CD8 +T cells in salivary glands. *Eur. J. Immunol.* **47**, 244–250 (2016).
- 924 45. E. Russo *et al.*, Intralymphatic CCL21 Promotes Tissue Egress of Dendritic Cells through Afferent
925 Lymphatic Vessels. *CellReports.* **14**, 1723–1734 (2016).
- 926 46. D. C. Marshall *et al.*, Selective Allosteric Inhibition of MMP9 Is Efficacious in Preclinical Models of
927 Ulcerative Colitis and Colorectal Cancer. *PLoS ONE.* **10**, e0127063–26 (2015).
- 928 47. J. Tønnesen, V. V. G. K. Inavalli, U. V. Nägerl, Super-Resolution Imaging of the Extracellular Space in
929 Living Brain Tissue. *Cell.* **172**, 1108–1121.e15 (2018).
- 930 48. A. Le, M. Saverin, A. R. Hand, Distribution of Dendritic Cells in Normal Human Salivary Glands. *Acta*
931 *Histochem. Cytochem.* **44**, 165–173 (2011).
- 932 49. F. Ginhoux, S. Jung, Monocytes and macrophages: developmental pathways and tissue homeostasis.
933 *Nat Rev Immunol.* **14**, 392–404 (2014).
- 934 50. S. Epelman, K. J. Lavine, G. J. Randolph, Origin and Functions of Tissue Macrophages. *Immunity.* **41**,
935 21–35 (2014).
- 936 51. Y. Lavin, A. Mortha, A. Rahman, M. Merad, Regulation of macrophage development and function in
937 peripheral tissues. *Nat Rev Immunol.* **15**, 731–744 (2015).
- 938 52. A. W. Roberts *et al.*, Tissue-Resident Macrophages Are Locally Programmed for Silent Clearance of
939 Apoptotic Cells. *Immunity.* **47**, 913–927.e6 (2017).
- 940 53. F. R. Stahl *et al.*, Nodular Inflammatory Foci Are Sites of T Cell Priming and Control of Murine
941 Cytomegalovirus Infection in the Neonatal Lung. *PLoS Pathog.* **9**, e1003828–18 (2013).
- 942 54. M. Baratin *et al.*, T Cell Zone Resident Macrophages Silently Dispose of Apoptotic Cells in the Lymph
943 Node. *Immunity*, 1–20 (2017).

- 944 55. S. Uderhardt, A. J. Martins, J. S. Tsang, T. Lämmermann, R. N. Germain, Resident Macrophages Cloak
945 Tissue Microlesions to Prevent Neutrophil-Driven Inflammatory Damage. *Cell*. **177**, 541–555.e17
946 (2019).
- 947 56. Y. Natsuaki *et al.*, Perivascular leukocyte clusters are essential for efficient activation of effector T
948 cells in the skin. *Nat Immunol*, 1–8 (2014).
- 949 57. K. W. Cho *et al.*, An MHC II-Dependent Activation Loop between Adipose Tissue Macrophages and
950 CD4+ T Cells Controls Obesity-Induced Inflammation. *CellReports*. **9**, 605–617 (2014).
- 951 58. T. A. Wynn, A. Chawla, J. W. Pollard, Macrophage biology in development, homeostasis and disease.
952 *Nature*. **496**, 445–455 (2013).
- 953 59. M. Hulsmans *et al.*, Macrophages Facilitate Electrical Conduction in the Heart. *Cell*. **169**, 510–
954 513.e20 (2017).
- 955 60. A. Scholer, S. Hugues, A. Boissonnas, L. Fetler, S. Amigorena, Intercellular adhesion molecule-1-
956 dependent stable interactions between T cells and dendritic cells determine CD8+ T cell memory.
957 *Immunity*. **28**, 258–270 (2008).
- 958 61. Z. Haimon *et al.*, Re-evaluating microglia expression profiles using RiboTag and cell isolation
959 strategies. *Nat Immunol*, 1–13 (2018).
- 960 62. P. Mrass *et al.*, CD44 Mediates Successful Interstitial Navigation by Killer T Cells and Enables Efficient
961 Antitumor Immunity. *Immunity*. **29**, 971–985 (2008).
- 962 63. G. Charras, E. Sahai, Physical influences of the extracellular environment on cell migration. *Nat Rev*
963 *Mol Cell Biol*. **15**, 813–824 (2014).
- 964 64. J. Renkawitz *et al.*, Nuclear positioning facilitates amoeboid migration along the path of least
965 resistance. *Nature*. **568**, 546–550 (2019).
- 966 65. M. G. Overstreet *et al.*, Inflammation-induced interstitial migration of effector CD4+ T cells is
967 dependent on integrin α V. *Nat Immunol*. **14**, 949–958 (2013).
- 968 66. A. Zaid *et al.*, Chemokine Receptor-Dependent Control of Skin Tissue-Resident Memory T Cell
969 Formation. *The Journal of Immunology*. **199**, 2451–2459 (2017).
- 970 67. Y.-J. Liu *et al.*, Confinement and Low Adhesion Induce Fast Amoeboid Migration of Slow
971 Mesenchymal Cells. *Cell*. **160**, 659–672 (2015).
- 972 68. V. Ruprecht *et al.*, Cortical Contractility Triggers a Stochastic Switch to Fast Amoeboid Cell Motility.
973 *Cell*. **160**, 673–685 (2015).
- 974 69. M. Bergert *et al.*, Force transmission during adhesion-independent migration. *Nat Cell Biol*. **17**, 524–
975 529 (2015).
- 976 70. K. Kendall, A. D. Roberts, van der Waals forces influencing adhesion of cells. *Philosophical*
977 *Transactions of the Royal Society B: Biological Sciences*. **370**, 20140078–20140078 (2014).
- 978 71. M. H. Lee, D. A. Brass, R. Morris, R. J. Composto, P. Ducheyne, The effect of non-specific interactions
979 on cellular adhesion using model surfaces. *Biomaterials*. **26**, 1721–1730 (2005).
- 980 72. R. J. Hawkins *et al.*, Pushing off the Walls: A Mechanism of Cell Motility in Confinement. *Phys. Rev.*
981 *Lett*. **102**, 1567–4 (2009).

- 982 73. T. Lämmermann *et al.*, Rapid leukocyte migration by integrin-independent flowing and squeezing.
983 *Nature*. **453**, 51–55 (2008).
- 984 74. K. Wolf *et al.*, Physical limits of cell migration: Control by ECM space and nuclear deformation and
985 tuning by proteolysis and traction force. *J Cell Biol.* **201**, 1069–1084 (2013).
- 986 75. R. G. Rowe, S. J. Weiss, Breaching the basement membrane: who, when and how? *Trends in Cell*
987 *Biology*. **18**, 560–574 (2008).
- 988 76. K. Wolf, Amoeboid shape change and contact guidance: T-lymphocyte crawling through fibrillar
989 collagen is independent of matrix remodeling by MMPs and other proteases. *Blood*. **102**, 3262–3269
990 (2003).
- 991 77. H. D. Hickman *et al.*, CXCR3 chemokine receptor enables local CD8(+) T cell migration for the
992 destruction of virus-infected cells. *Immunity*. **42**, 524–537 (2015).
- 993 78. S. Halle *et al.*, In Vivo Killing Capacity of Cytotoxic T Cells Is Limited and Involves Dynamic
994 Interactions and T Cell Cooperativity. *Immunity*. **44**, 233–245 (2016).
- 995 79. B. C. Schaefer, M. L. Schaefer, J. W. Kappler, P. Marrack, R. M. Kedl, Observation of antigen-
996 dependent CD8+ T-cell/ dendritic cell interactions in vivo. *Cell Immunol.* **214**, 110–122 (2001).
- 997 80. A. C. Kirby, M. C. Coles, P. M. Kaye, Alveolar Macrophages Transport Pathogens to Lung Draining
998 Lymph Nodes. *J. Immunol.* **183**, 1983–1989 (2009).
- 999 81. A. J. Ozga *et al.*, pMHC affinity controls duration of CD8 +T cell–DC interactions and imprints timing
1000 of effector differentiation versus expansion. *J. Exp. Med.* **213**, 2811–2829 (2016).
- 1001 82. R. L. Lindquist *et al.*, Visualizing dendritic cell networks in vivo. *Nat Immunol.* **5**, 1243–1250 (2004).
- 1002 83. B. Stolp *et al.*, HIV-1 Nef interferes with T-lymphocyte circulation through confined environments in
1003 vivo. *Proceedings of the National Academy of Sciences*. **109**, 18541–18546 (2012).
- 1004 84. M. Vladymyrov, J. Abe, F. Moalli, J. V. Stein, A. Ariga, Real-time tissue offset correction system for
1005 intravital multiphoton microscopy. *Journal of Immunological Methods*. **438**, 35–41 (2016).
- 1006 85. A. Marquardt *et al.*, Single cell detection of latent cytomegalovirus reactivation in host tissue.
1007 *Journal of General Virology*. **92**, 1279–1291 (2011).
- 1008 86. L. G. Guidotti *et al.*, Immunosurveillance of the Liver by Intravascular Effector CD8+ T Cells. *Cell*. **161**,
1009 486–500 (2015).
- 1010 87. P. Paul-Gilloteaux *et al.*, eC-CLEM: flexible multidimensional registration software for correlative
1011 microscopies. *Nat Meth.* **14**, 102–103 (2017).

1012

Figure legends

Fig. 1. Dynamic motility parameters of memory CD8⁺ T cells in PLN versus SMG. **A.** Experimental layout for CD8⁺ T cell analysis in SMG and PLN. **B.** Immunofluorescent sections of GFP⁺ OT-I T cells in PLN and SMG in memory phase (\geq day 30 p.i.). Scale bar, 100 μ m (left panels) and 20 μ m (right panel). **C.** Time-lapse 2PM image sequences showing OT-I CD8⁺ T_{PLN-M} cell motility in PLN in memory phase (\geq day 30 p.i.). **D and E.** Time-lapse 2PM image sequences showing OT-I CD8⁺ T_{RM} cell motility in SMG in memory phase (\geq day 30 p.i.). Arrowheads indicate protrusions (**D**) and the arrow indicates squeezing behavior (**E**) of OT-I CD8⁺ T_{RM}. Scale bar in C-E, 10 μ m. Time in min:s. **F.** Time-coded shapes of exemplary T_{PLN-M} and T_{RM} tracks. **G.** Shape factor distribution of T_{PLN-M} and T_{RM} with exemplary cell shapes. **H.** Speed frequency distribution of OT-I CD8⁺ T cells in PLN and SMG. Arrows indicate median values (μ m/min). **I.** Arrest coefficient frequency distribution of OT-I CD8⁺ T cells in PLN and SMG (cut-off < 2.5 μ m/min). **J.** Mean displacement versus time of OT-I T_{PLN-M} (left) and T_{RM} (right) before and after OVA₂₅₇₋₂₆₄ injection with motility coefficients (μ m²/min). **K.** IFN- γ expression in OT-I T_{PLN-M} and T_{RM} 24 h after OVA₂₅₇₋₂₆₄ injection (mean \pm SD). Data in G are from 2-3 independent experiments and 3 mice total for each group. Data in H and I are pooled from 5 to 6 mice from 4 independent experiments with at least 194 tracks analyzed per organ. Data in J are pooled of 3-4 mice from 2 independent experiments. Data in K show one of two independent experiments. Data in G and I were analyzed with Mann-Whitney-test and data in H with Student's t-test. ***, p < 0.001.

Fig. 2. SMG T_{RM} move alongside tissue macrophages. **A.** Immunofluorescent section showing localization of SMG T_{RM} adjacent to tissue macrophages (arrows). Scale bars, 1 mm (left), 100 μ m (middle) and 20 μ m (right). **B.** Percent of SMG T_{RM} adjacent to tissue macrophages. Data are pooled from 105 FOV with a total of 3270 T_{RM} and shown as box and whisker graph with 2.5 – 97.5 percentiles. **C.** Correlative light and electron microscopy sections (left; confocal image; middle and right, TEM image) showing close spatial association of SMG T_{RM} and tissue macrophages. M, tissue macrophages; E, epithelial cell; ME, myoepithelial cell; ECM, extracellular matrix. Scale bar, 5 (left), 2 (middle) and 1 μ m (right). **D.** TEM images showing attachment of epithelial cells to ECM (top) and through intercellular junctions (white arrows; bottom). Scale bar, 800 nm. **E.** 2PM time-lapse image sequence showing overlap of OT-I T_{RM} tracks with tissue macrophages in SMG in

memory phase (\geq day 30 p.i.). Scale bar, 20 μ m. Time in min:s. The right panels show the time accumulated overlays of images with or without OT-I T_{RM} . **F.** Immunofluorescent section of WT and CXCR3^{-/-} OT-I T cells and macrophages. Magnified image shows association of CXCR3^{-/-} OT-I T_{RM} to tissue macrophages (arrows). Scale bar, 100 μ m (left) and 20 μ m (right).

1044

Fig. 3. Confinement induces SMG T_{RM} motility through chemokine- and adhesion-mediated signals and bivalent cation-dependent friction. **A.** Experimental layout of under agarose assay. Arrows indicate F-actin flow. **B.** Representative T_N (n = 75) and T_{RM} (n = 58) tracks in presence of chemokine and ICAM-1. **C.** Speeds of T_N and T_{RM} . Data are presented as Tukey box and whiskers plot. **D.** Time-lapse image sequence showing T_{RM} motility among immotile T_N . T_{RM} displacement shown by segmented line. Scale bar, 20 μ m. Time in min:s. **E.** Time-lapse image sequence in under agarose plates coated with HSA showing T_{PLN-M} (top) and T_{RM} (bottom) motility. Cell displacement shown by segmented line. Scale bar, 10 μ m. Time in min:s. **F.** Representative T_N (n = 75), T_{PLN-M} (n = 226) and T_{RM} (n = 379) tracks. **G.** T_N , T_{PLN-M} and T_{RM} speeds in under agarose plates coated with HSA. Numbers indicate percentage of tracks > 3 μ m/min (boxed). Lines indicate median. **H.** Meandering index of T_N , T_{PLN-M} and T_{RM} tracks. **I.** T_{RM} speeds after treatment with PTx, RGD peptide, anti-Mac1 mAb, or in presence of EDTA. Numbers indicate percentage of tracks > 3 μ m/min (boxed). Lines indicate median. **J.** Image sequence of T_{RM} protrusions in presence of EDTA. Scale bar, 10 μ m. **K.** Representative T_{RM} cell tracks in presence of EDTA (n = 75). **L.** Mean displacement over time of T_{RM} tracks. Numbers indicate motility coefficients (μ m²/min). Data in C, G, H, I and L were pooled from at least 2 independent experiments each. Statistical analysis was performed with unpaired t-test (C) or Kruskal-Wallis with Dunn's multiple comparison in G - I (as compared to " T_{RM} "). **, p < 0.01; ***, p < 0.001.

1061

Fig. 4. T_{RM} insert protrusions for cell displacement in absence of external chemoattractants and friction. **A.** Experimental layout. Arrows indicate protrusion direction. **B.** Image sequences of T_{RM} within T_N clusters in presence of EDTA. Arrowheads show membrane protrusions; segmented line indicates cell track. Scale bar, 10 μ m. Time in min:s. **C.** Graphical representation of T_{RM} inside T_N cluster (i) or dispersed (ii). **D.** T_{RM} track speeds according to their location. Numbers indicate percentage of tracks > 3 μ m/min (boxed). Lines indicate

1067 median. **E.** Meandering index of T_{RM} tracks sorted according to their location. Lines indicate median. **F.** Image
 1068 sequences of T_{RM} alone (top) and with 7 μ m polystyrene beads (bottom) in presence of EDTA. Arrowheads
 1069 show membrane protrusions. Segmented line indicates cell track. Scale bar, 10 μ m, time in min:s. **G.** T_{RM} track
 1070 speeds according to their association with or without beads. Numbers indicate percentage of tracks > 3
 1071 μ m/min (boxed). Lines indicate median. **H.** Meandering index of T_{RM} tracks sorted according to their location.
 1072 Lines indicate median. Data in D, E, G and H are pooled from 4 - 5 independent experiments. Statistical
 1073 analysis was performed with Mann-Whitney test. ***, $p < 0.001$.

1074

1075 **Fig. 5. Residual *in vivo* SMG T_{RM} motility during inhibition of $G_{\alpha i}$ and integrins.** **A.** Experimental layout. **B.**
 1076 OT-I T_{PLN-M} and T_{RM} speeds after combined anti- αL , $\alpha 4$ and αE integrin mAb (αItg) inhibition. Arrows indicate
 1077 median values (μ m/min). **C.** 2PM image of T_{RM} – tissue macrophage colocalization in αItg -treated SMG.
 1078 Arrows indicate T cell – tissue macrophage contacts. Scale bar, 20 μ m. **D.** OT-I T_{RM} speeds in SMG after WD
 1079 administration of RAD or RGD peptide. **E.** WT and CXCR3^{-/-} OT-I T_{RM} speeds in SMG in memory phase (\geq day
 1080 30 p.i.). Arrows indicate median values (μ m/min). **F.** OT-I T_{PLN-M} and T_{RM} speeds after systemic treatment with
 1081 active PTx or inactive (mutant) PTx (PTx_{mut}). Arrows indicate median values (μ m/min). **G.** 2PM image of T_{RM} –
 1082 tissue macrophage colocalization in PTx-treated SMG. Arrows indicate T cell – tissue macrophage contacts.
 1083 Scale bar, 20 μ m. **H.** Flow cytometry plot of mixed T_{RM} and macrophages. **I.** Quantification of cluster formation
 1084 as shown in H. **J.** Example image sequences showing T_{RM} in transient contact with macrophages under agarose
 1085 on fibronectin-coated plates. T_{RM} displacement is shown by segmented line. Scale bar, 50 μ m. Time in min:s.
 1086 **K.** T_{RM} – macrophage contact duration for individual tracks. Data in B, D, E and F are pooled from 2-5
 1087 independent experiments with a total of 2-7 mice with at least 111 tracks per condition and analyzed with
 1088 unpaired Student's t-test. Data in I are pooled from 2 independent experiments and analyzed using unpaired
 1089 Student's t-test. ***, $p < 0.001$.

1090

1091 **Fig. 6. Tissue macrophage attachment in SMG.** **A.** Experimental layout of super-resolution shadow imaging
 1092 (SUSHI) of SMG slices. **B.** Example of SUSHI image for determination of extracellular space. E, epithelium; BV,
 1093 blood vessel. Scale bar, 10 μ m. **C.** Overview of ECS signal with SMG epithelium (E) and CD11c-YFP⁺ tissue

1094 macrophages. Scale bar, 10 μ m. **D.** Example of epithelial attachment before and after hyperosmotic
 1095 challenge. Arrows show interepithelial junctions. Scale bar, 5 μ m. **E.** Example of macrophage detachment
 1096 before and after hyperosmotic challenge. Arrowheads indicate detachment. Scale bar, 5 μ m. **F.**
 1097 Quantification of gap size between macrophage and epithelium before and after hyperosmotic challenge. **G.**
 1098 Immunofluorescent SMG section showing macrophages and epithelial cells in acini and ducts (identified by
 1099 luminal ZO-1 labelling). Yellow dashed lines indicate outlines of acini and ducts. Scale bar, 10 μ m. **H.** Confocal
 1100 image of SMG section with macrophage protrusions traversing a basement membrane below an epithelial
 1101 acinus (indicated by arrow). Scale bar, 20 μ m (overview) and 5 μ m (insert). **I.** Electron microscopy image of
 1102 macrophages creating a discontinuation of the basement membrane of an acinus (indicated by arrow).
 1103 Numbers mark two neighboring macrophages. Arrowheads indicate lack of tight adhesion between
 1104 macrophages and neighboring cells. Scale bar, 2 μ m. All images are representative of at least 2 independent
 1105 experiments. Data in F were analyzed using a paired t-test. ***, $p < 0.001$.

1106

1107 **Fig. 7. Tissue macrophages assist T_{RM} patrolling of SMG.** **A.** 2PM time-lapse image sequence of T_{RM} in DTx-
 1108 treated CD11c-YFP or CD11c-DTR \rightarrow Ubi-GFP chimeras. Magenta lines indicate outlines of acini, white
 1109 segmented lines indicate cell tracks. Scale bar, 50 μ m (overview) and 20 μ m (insert). Time in min:s. **B.** Example
 1110 T_{RM} tracks in presence or absence of macrophage. Scale bar, 10 μ m. **C.** Frequency distribution of T_{RM} speeds
 1111 in DTx-treated CD11c-YFP or CD11c-DTR bone marrow chimera. Arrows indicate median (μ m/min). **D.** Track
 1112 analysis outline. Top panel. U-turns (red) describe tracks reversing direction while excluding continuous
 1113 turns. Bottom panel. Synthetic tracks were generated to assess dwell time in an 80 μ m-diameter sphere
 1114 (black). One example track is shown for control (light blue) and macrophage-depleted (dark blue) condition.
 1115 **E.** Percent of tracks making U-turn. Bars indicate 95% confidence intervals. **F.** *In silico* dwell times for T_{RM}
 1116 tracks in 80 μ m-spheres based on measured track parameters. **G.** 2PM time-lapse image sequences of T_{RM}
 1117 crawling along a macrophage to enter acini. Epithelial signal was manually masked to show an isolated acinus
 1118 in zoomed panels. Dashed white line indicates area displayed in xz-view, and arrow indicates T_{RM} -
 1119 macrophage contact. Top: Scale bar, 50 μ m (overview) and 20 μ m (insert); bottom: Scale bar, 20 μ m
 1120 (overview) and 10 μ m (insert). Time in min:s. **H.** Percentage of T_{RM} transitions into or out of acini and ducts

1121 in CD11c-YFP -> Ubi-GFP chimeras (n = 42) with and without contact to macrophages. **I, J.** 2PM time-lapse
 1122 image sequence of CD11cYFP -> Ubi-GFP and DTx-treated CD11cDTR->Ubi-GFP chimeras were analyzed for
 1123 T_{RM} crossing events (leaving or entering acini). **I** shows average transitions per hour track duration, and **J**
 1124 depicts transitions per 1000 μm total distance migrated. Data points represent individual image sequences.
 1125 Line indicates mean. **K.** Experimental layout for analysis of T_{RM} response to local chemokine. CXCL10 was
 1126 injected with a fluorescent tracer for 4 h to allow T_{RM} accumulation. Integrin blocking mAbs prevent
 1127 recruitment of circulating T cells. **L.** T_{RM} per cm^2 at sites of CXCL10 injection in presence or absence of
 1128 macrophages. Numbers indicate mean \pm SD. Data in C, I, J and L are pooled from 2-4 independent
 1129 experiments with 4-6 mice total. Data in C, I and J were analyzed with Mann-Whitney and data in L were
 1130 analyzed with Wilcoxon rank test. *, $p < 0.05$; ***, $p < 0.001$.

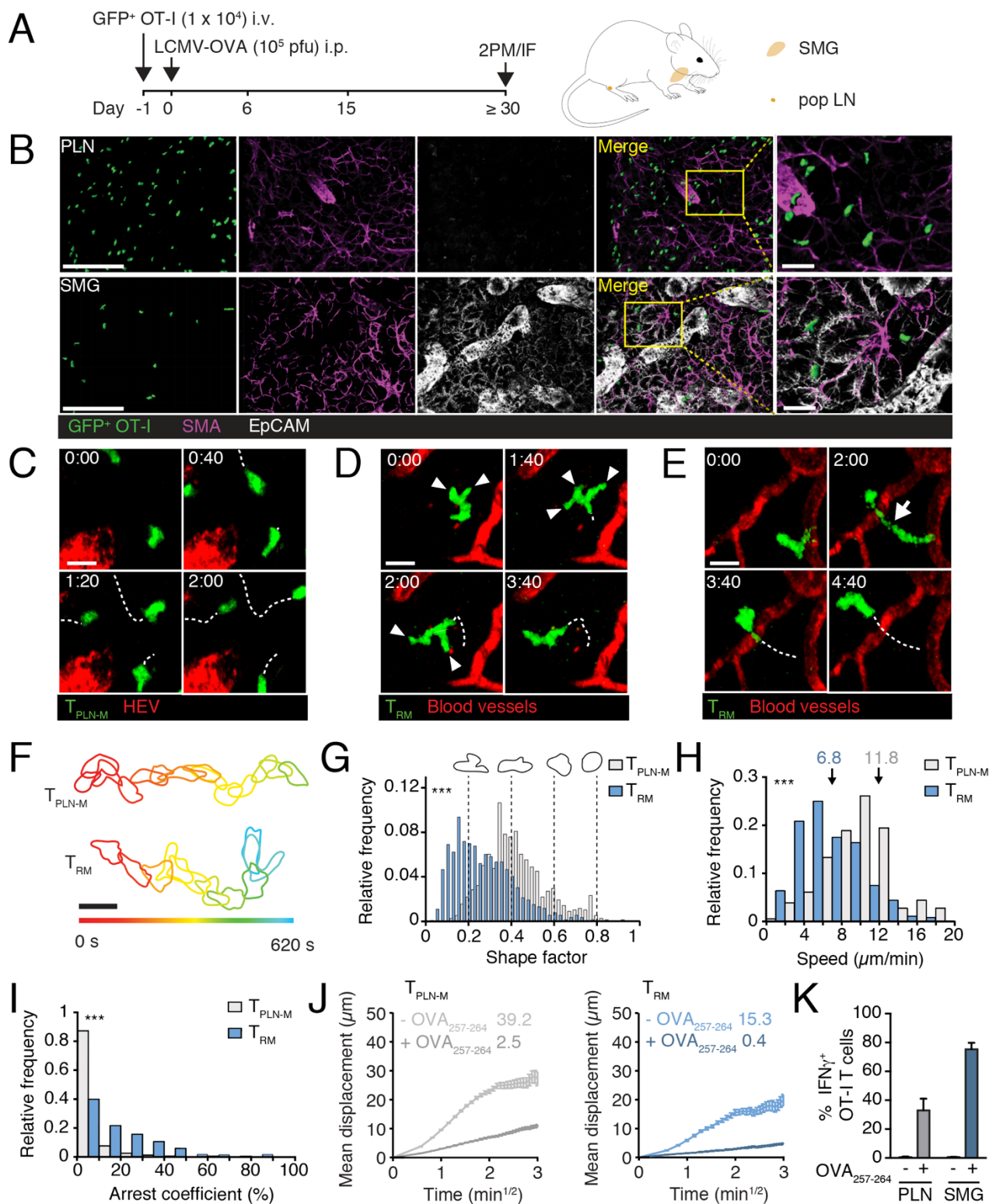


Figure 1

1131

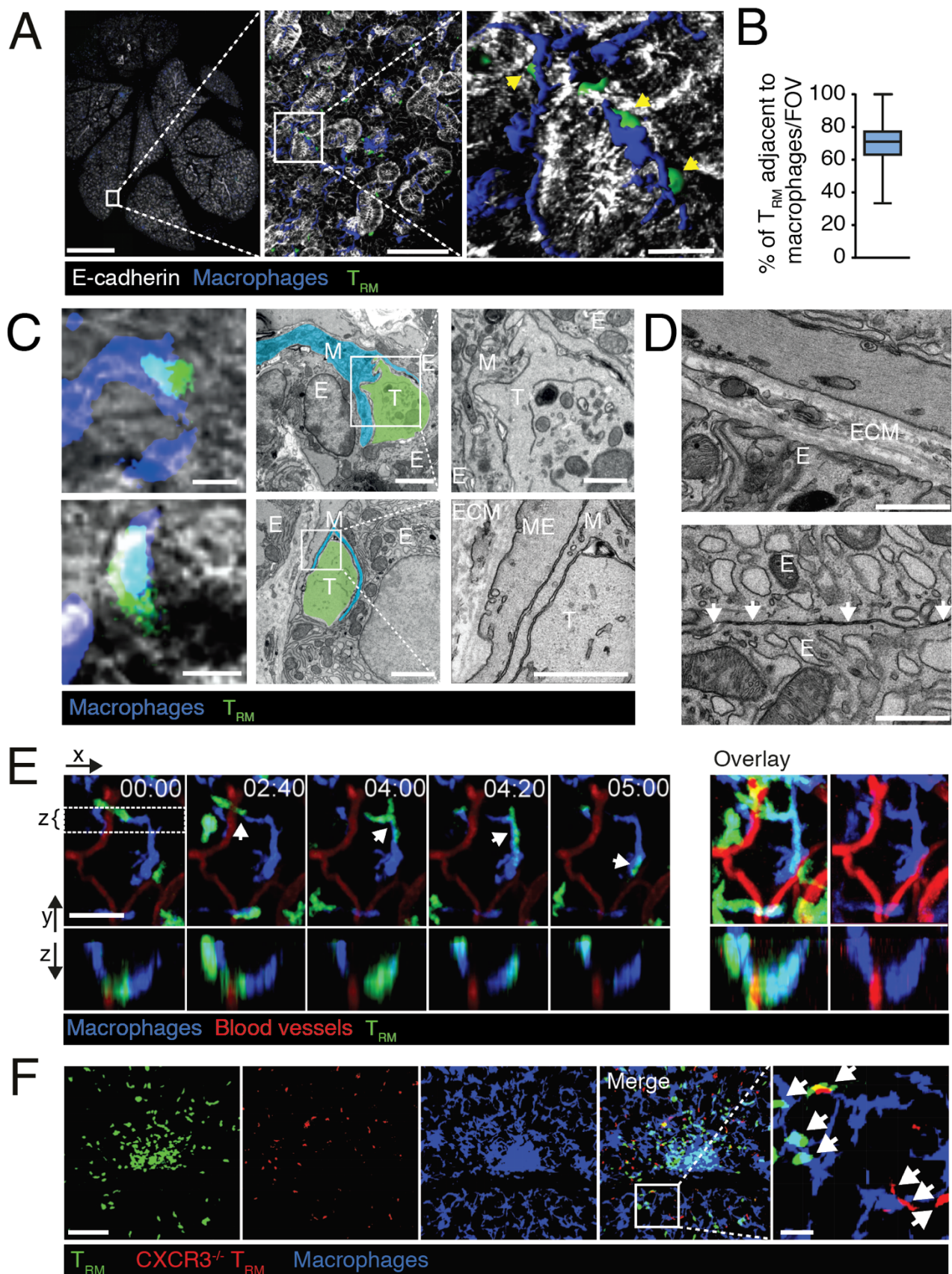


Figure 2

1132

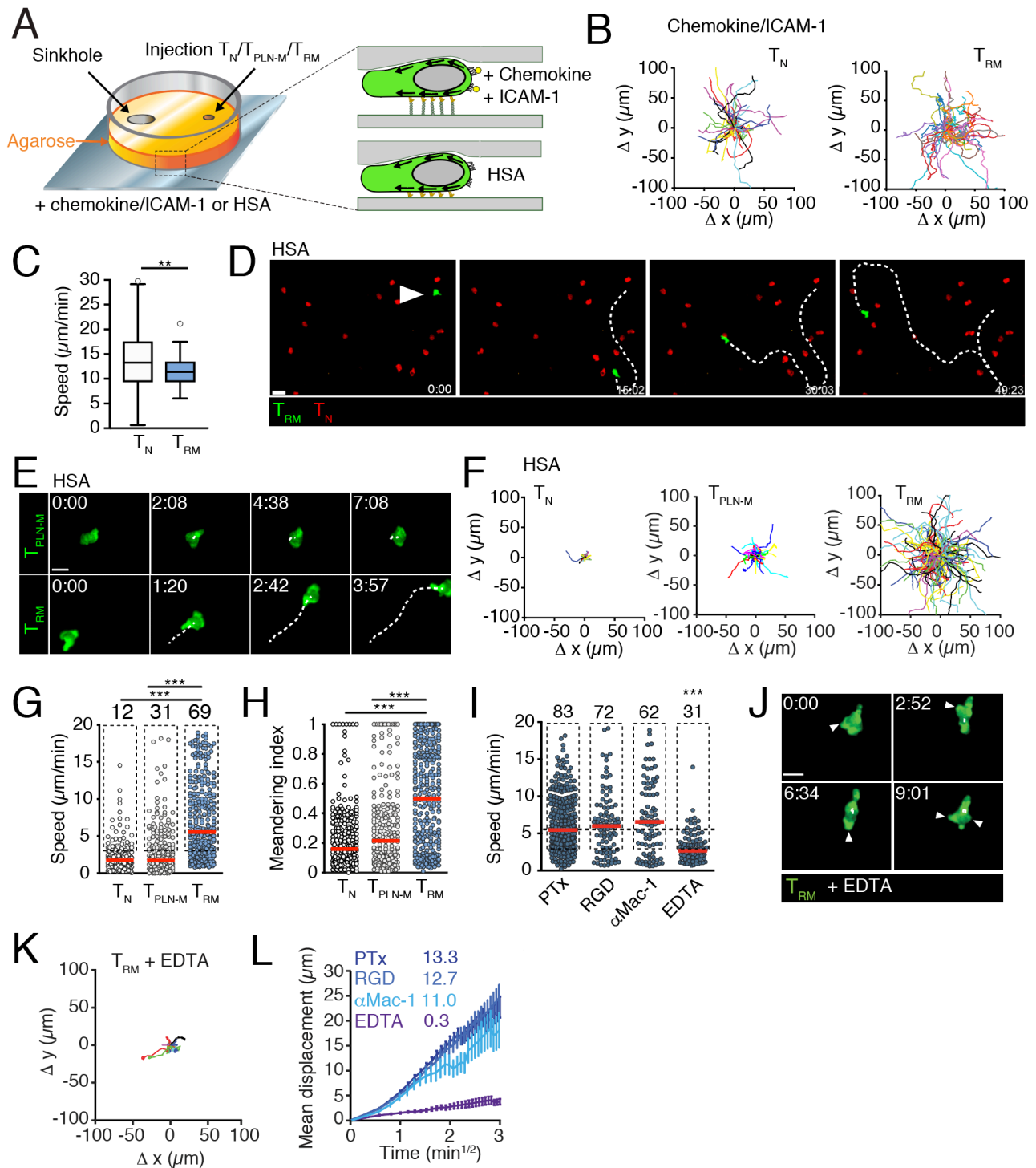


Figure 3

1133

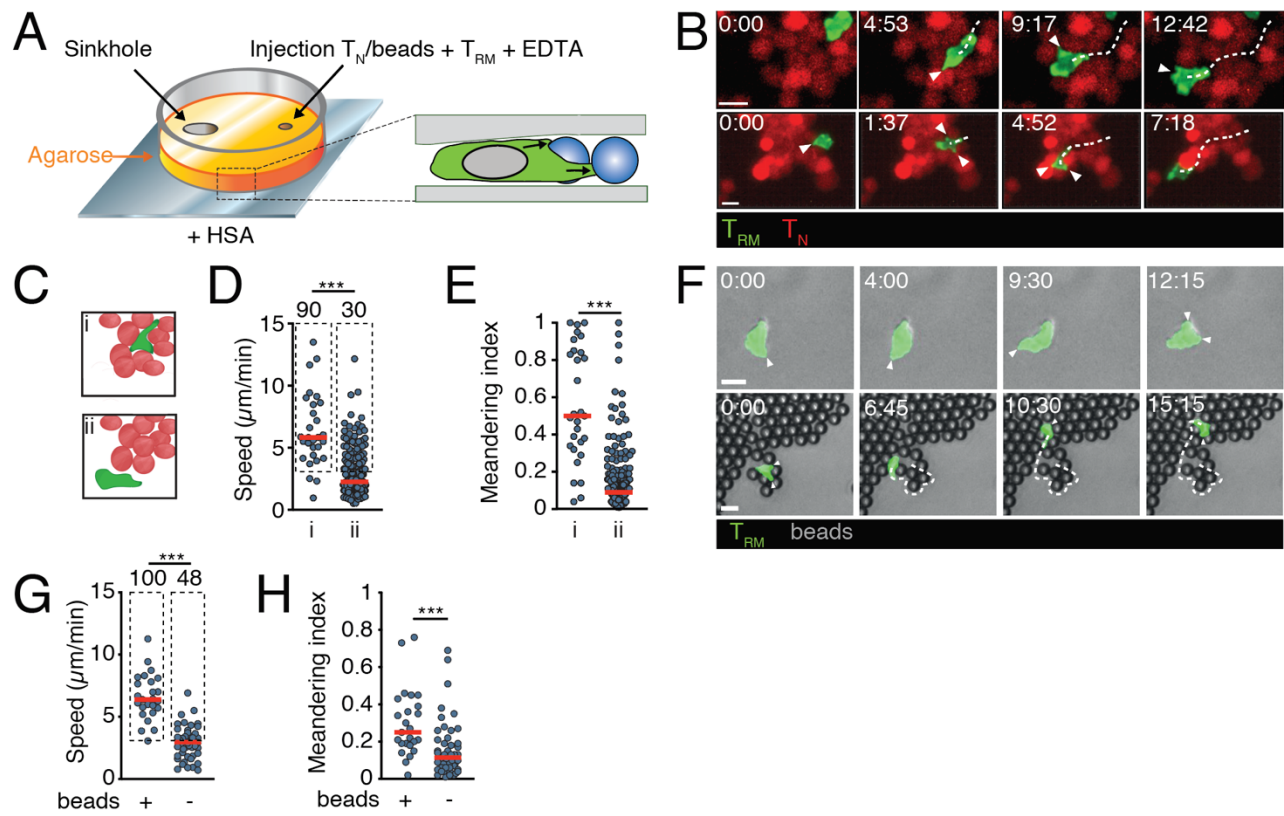


Figure 4

1134

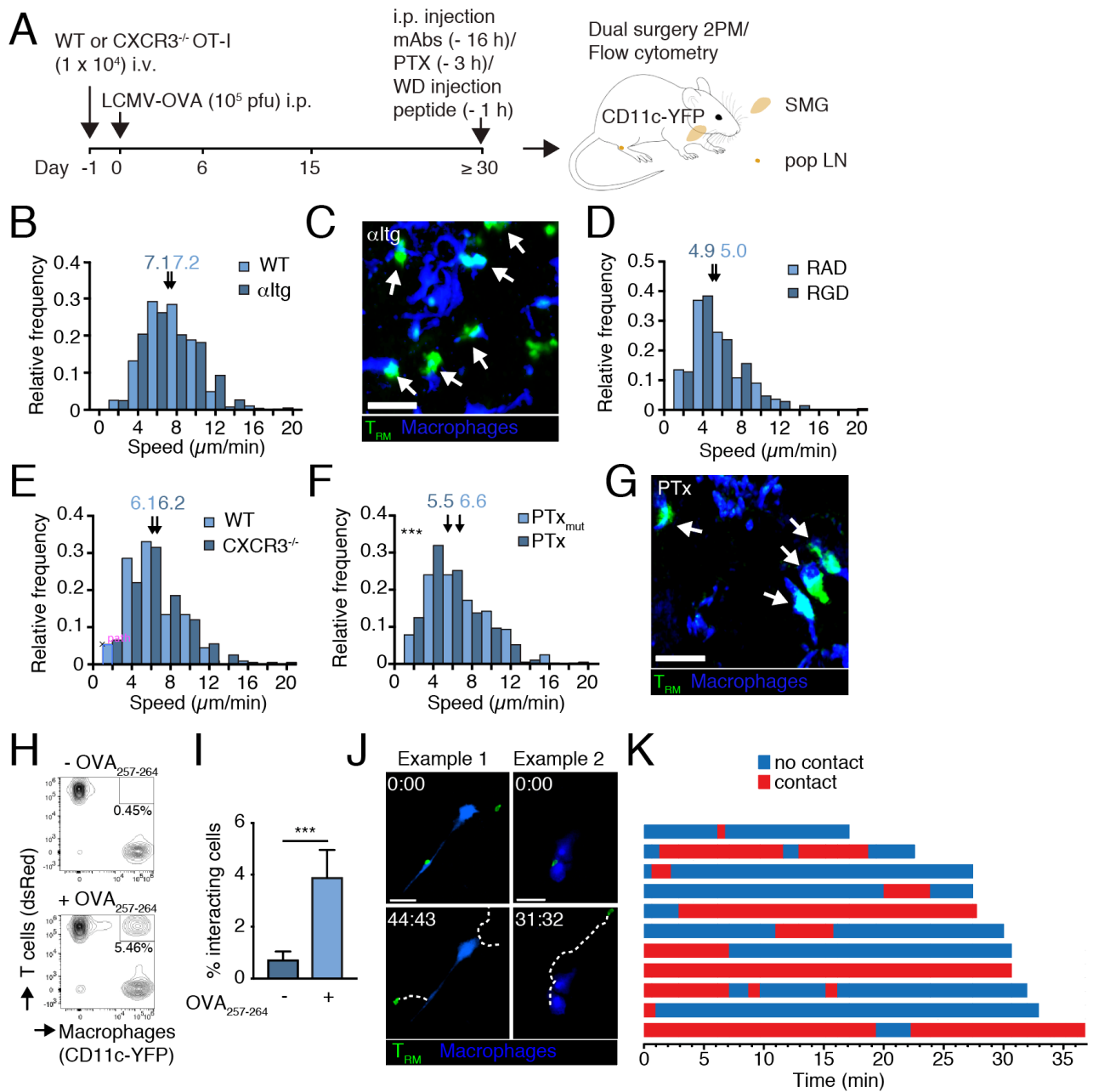
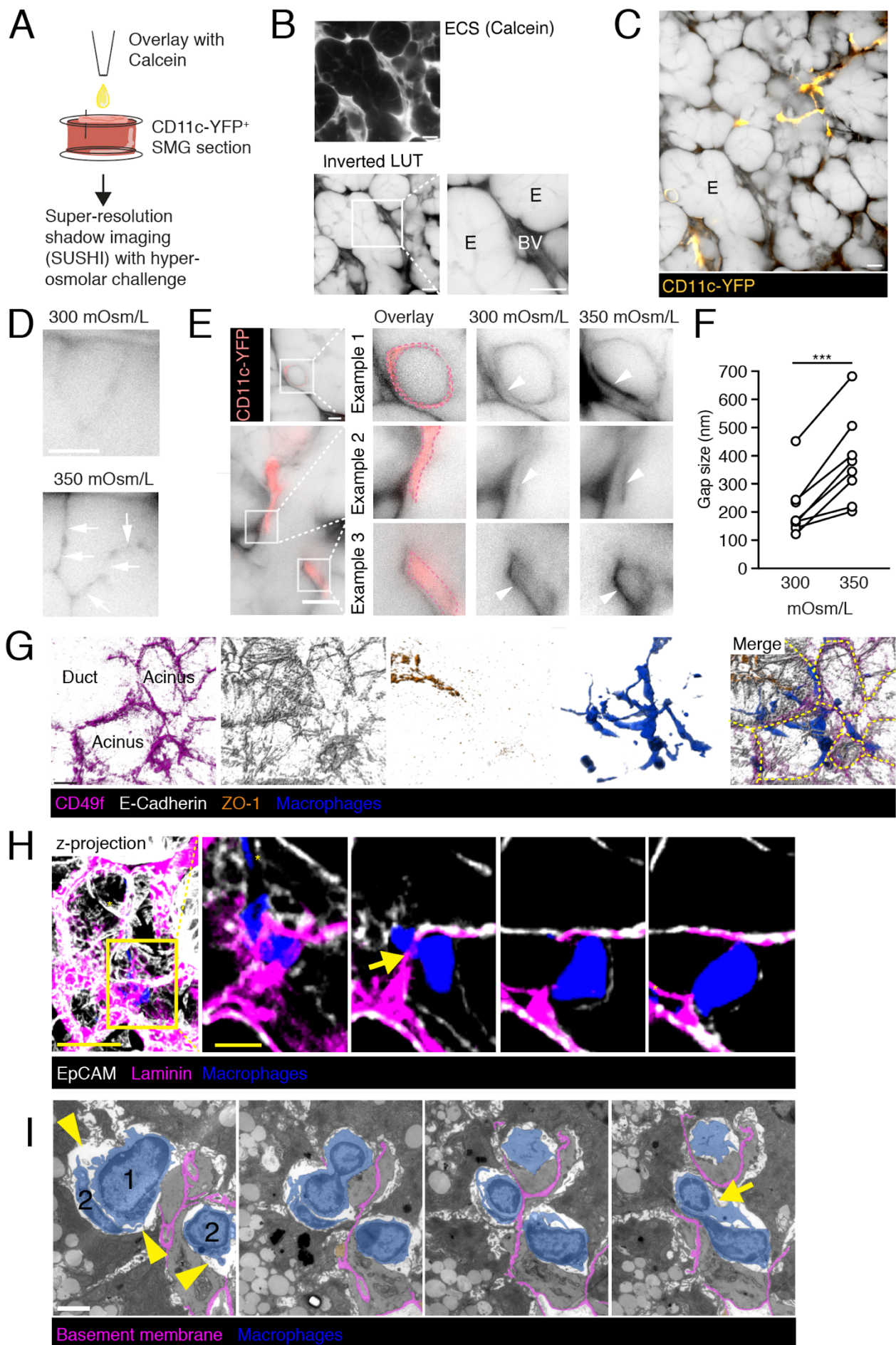


Figure 5

1135



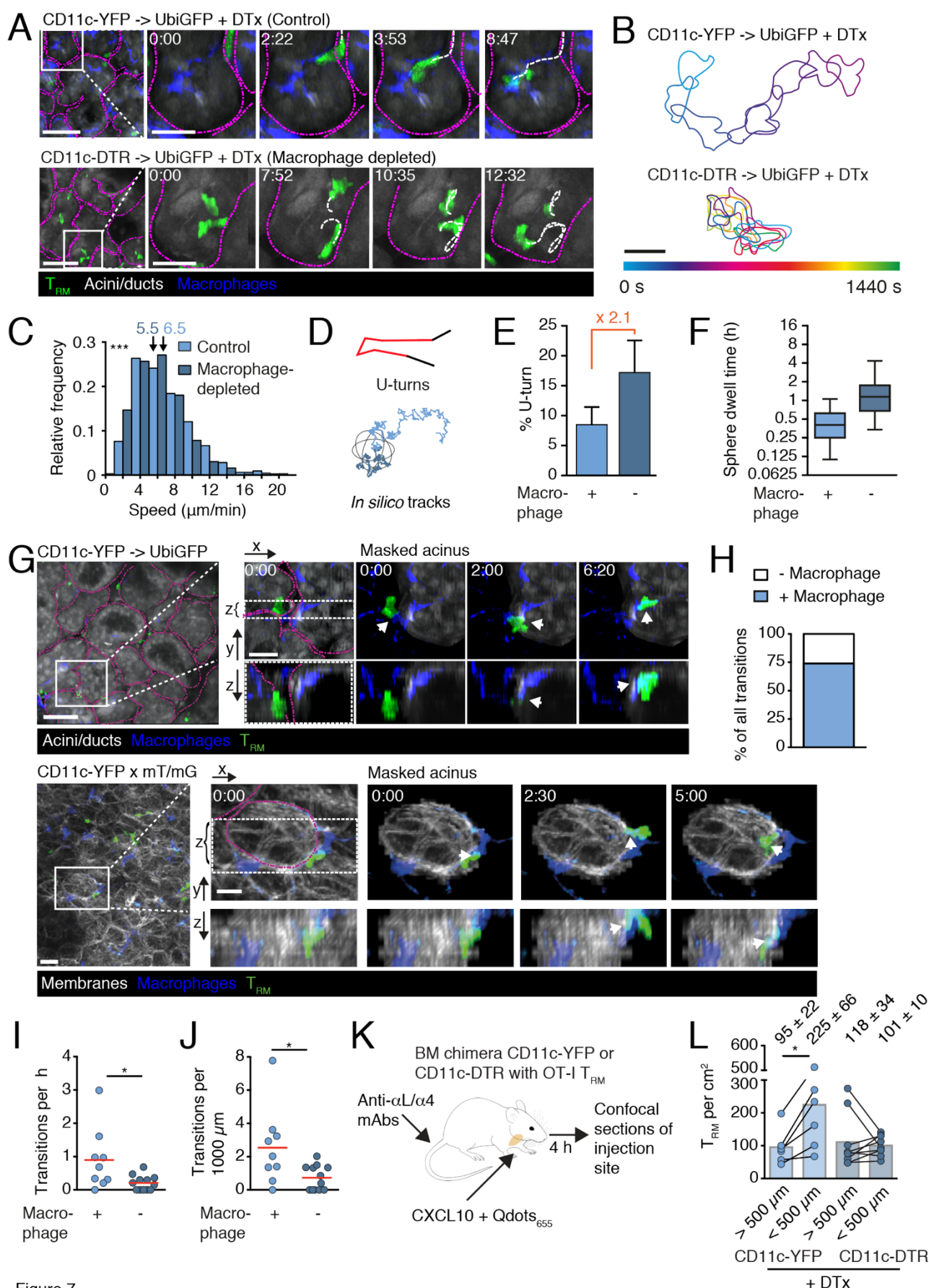


Figure 7